University of Kent

Kent Academic Repository

Pengfei, Zhu, Zhen, Wu, Huan, Wang, Yan, Hongli, Bo, Li, Yang, Fusheng and Zhang, Zaoxiao (2022) ***Ni coarsening and performance attenuation prediction of biomass syngas fuelled SOFC by combining multi-physics field modelling and artificial neural network.*** **Applied Energy, 322 . ISSN 0306-2619.**

Downloaded from

https://kar.kent.ac.uk/93978/ The University of Kent's Academic Repository KAR

The version of record is available from

https://doi.org/10.1016/j.apenergy.2022.119508

This document version

Author's Accepted Manuscript

DOI for this version

Licence for this version

UNSPECIFIED

Additional information

Versions of research works

Versions of Record

If this version is the version of record, it is the same as the published version available on the publisher's web site. Cite as the published version.

Author Accepted Manuscripts

If this document is identified as the Author Accepted Manuscript it is the version after peer review but before type setting, copy editing or publisher branding. Cite as Surname, Initial. (Year) 'Title of article'. To be published in ***Title of Journal*** , Volume and issue numbers [peer-reviewed accepted version]. Available at: DOI or URL (Accessed: date).

Enquiries

If you have questions about this document contact ResearchSupport@kent.ac.uk. Please include the URL of the record in KAR. If you believe that your, or a third party's rights have been compromised through this document please see our Take Down policy (available from https://www.kent.ac.uk/guides/kar-the-kent-academic-repository#policies).

Ni coarsening and performance attenuation prediction of biomass syngas fueled SOFC by combining multi-physics field modeling and artificial neural network

Pengfei Zhu[a], Zhen Wu[a]*, Huan Wang[a], Hongli Yan[b], Bo Li[c], Fusheng Yang[a], Zaoxiao Zhang[a,d]

[a]School of Chemical Engineering and Technology, Xi'an Jiaotong University, Xi'an, 710049, China

[b]Department of Mechanical Engineering, Xi'an Jiaotong University City College, Xi'an, 710018, China

[c]School of Engineering, University of Kent, Kent CT2 7NZ, UK

[d]State Key Laboratory of Multiphase Flow in Power Engineering, Xi'an Jiaotong University, Xi'an, 710049, China

Corresponding author: wuz2015@mail.xjtu.edu.cn (Z. Wu)

Abstract: Ni particle coarsening is an important factor in deteriorating the durability of solid oxide fuel cell (SOFC) operations. In order to investigate the influence of Ni coarsening on SOFC performance, the transient multi-physical field model of SOFC was developed in this paper. The high operating temperature accelerates Ni particle growth and increases the attenuation rate of SOFC current density from 0.23%/kh at 650 ºC to 2.6%/kh at 800 ºC. The increase in the ratio of steam to carbon also intensifies the Ni particle coarsening process and deteriorates the transient performance of SOFC. Increasing YSZ particle diameter could hinder the growth of Ni particles and slowing down the increase rate of Ni particle diameter. Within the range of preset YSZ diameter d_{YSZ}, increasing d_{YSZ} reduces the attenuation rate and increases the average current density. Improving Ni phase fraction helps to reduce the attenuation rate of current density. Since multi-physical field (MPF) simulation needs long calculation time and it is difficult to achieve fast prediction, artificial neural network (ANN) is trained by the database generated by MPF. The mapping relationship between operating parameters, structural parameters and attenuation indexes is obtained. Finally, the attenuation performance of SOFC is optimized by genetic algorithm (GA) through data-driven method. The absolute average relative errors of all parameters in predicting attenuation rate and average current density are as low as 0.767% and 0.248%, which indicates the reliability of the ANN prediction. After optimization, the maximum current density is 5960 $A \cdot m^{-2}$ under operating voltage at 0.6 V when the attenuation rate requirement not exceeding 1% is satisfied. The combination of MPF simulation, ANN and GA

The short version of the paper was presented at ICAE2021, Nov 29-Dec 5. This paper is a substantial extension of the short version of the conference paper.

provides a framework for fast performance prediction and optimization of strong nonlinear system.

Keywords: Solid oxide fuel cell, Ni coarsening, Multi-physics field, Artificial neural network, Performance attenuation prediction

Nomenclature

Abbreviations

AFL	Anode functional layer
ANN	Artificial neural network
ASL	Anode support layer
BRFS	Binary random filled sphere
CCCL	Cathode current collector layer
CFL	Cathode functional layer
DPB	Double phase boundary
EL	Electrolyte layer
FC	Fuel cell
GA	Genetic algorithm
MPF	Multi-physics filed
MSE	Mean square error
MSR	Methane steam reforming
RM	Reverse methanation
SOFC	Solid oxide fuel cell
TPB	Triple phase boundary
WGS	Water gas shift

Symbols

A	Specific surface area
d	Thickness or diameter
D	Diffusion coefficient
E_{act}	Activation energy
E_{eq}	Equilibrium potential
F	Faraday constant
j	Volume current density or mass diffusion flux
k	Reaction rate constant
K	Adsorption constant
K_{eq}	Reaction equilibrium constant
L	Cell length
M	Molar mass
N	Total number of particles
p	Partial pressure
P	Percolation probability
Q_m	Source term
R	Reaction rate or Ideal gas constant
r	Radius or attenuation rate
u	Velocity
V	Output voltage
y	Molar fraction
Z	Coordination number
w	TPB active width
$\bar{I}$	Average current density

Greek letters

α	Charge transfer coefficient or Bruggeman factor
γ	Pre-exponential factor
ε	Porosity
η	Effectiveness factors
θ	Contact angle
κ	Permeability
λ	TPB area
μ	Dynamic viscosity
ξ	Number fraction of particles
ρ	Density
σ	Electrical conductivity
ψ	Phase volume
ω	Mass fraction

Subscripts and superscripts

0	Initial state
20 K	Twenty thousands
eff	Effective
el	Electronic phase
el-el	Electronic phase-electronic phase
el-io	Electronic phase-ionic phase
io	Ionic phase
io-el	Ionic phase-electronic phase
io-io	Ionic phase-ionic phase
O	Oxide
R	Reduction

1. Introduction

As the concept of environmental protection is deeply rooted into the hearts of the people, countries around the world pay more and more attention to CO_2 emission reduction. For example, China explicitly proposed the dual carbon goals of "peak carbon" by 2030 and "carbon neutral" by 2060 in September 2020 [1,2]. Besides, more than 50 countries, including Germany, France and the European Union have also pledged to reach net zero emissions by mid-century [3]. This means that reducing CO_2 emissions is imminent and the pace of carbon reduction needs to be accelerated [4]. Under the strong demand of the current carbon reduction target, clean and efficient energy conversion technology has become a hot topic in current research.

Solid oxide fuel cell (SOFC), as a kind of high temperature fuel cell (FC), is regarded as the next power generation technology due to its superior performance [5]. First, SOFC directly converts the chemical energy of fuel into electrical energy through electrochemical reaction, which is different from the traditional chemical-mechanical-electrical energy conversion path for power generation. The maximum electrical efficiency of SOFC is not limited by the traditional Carnot cycle [6], which is also one of SOFC's outstanding strengths: high efficiency. In addition, SOFCs usually operate at 600-1000 ^oC [7], which is also why the SOFC is categorized as high temperature FC. High temperature operation enables SOFCs to have a wide range of fuel selectivity, because the reforming and shift reactions occurs under such high temperature, which could convert hydrocarbons [8,9], alcohols [10,11], ammonia [12,13], and even solid biomass [14,15] into H_2 and CO for electrochemical reactions. In particular, biomass-based SOFC is possible to achieve net zero CO_2 emissions, which is of great significance for reducing CO_2 emission. Therefore, biomass-based SOFC is of great interest to many researchers. There have been numerous works discussing the biomass-based SOFC performance at the cell and system levels. Another advantage of high temperature operation of SOFC is that it improves the electrochemical reaction rate in the case of avoiding the use of precious metal catalysts such as Pt and Rh, which eliminates catalyst poisoning to operate more stably [16]. It is worth mentioning that SOFC also has some engineering merits, such as low noise, high modularity, flexible installation position, etc., which helps to promote the SOFC practical application.

Although the above analyses show the strong vitality of SOFC as a clean energy conversion technology, SOFC still faces some problems and challenges in the aspect of stable operation. At present, the stabilization operation requirement of commercial SOFC is that the performance attenuation rate

keeps less than 1%/1000 h and the lifetime extends more than 40,000 h under stationary application scenarios [17,18]. The factors affecting SOFC performance attenuation can be divided into two aspects, namely mechanical damage and material degradation. The mechanical damage is the main mechanism of SOFC performance attenuation caused by physical action. The mechanical damage means the damage of the SOFC mechanical structure, including cracking, delamination, creep damage, etc., which is mainly caused by thermal stress [19]. The main countermeasures include minimizing temperature gradient, optimizing structure design and material selection. The material degradation can be divided into four types according to different positions: cathode, electrolyte, interconnect and anode. The main reason of cathode material degradation is that Cr and Zr series oxides generated in the cathode block the active site of electrochemical reaction, hinder the adsorption and diffusion of gas, increase the ohm resistance thus to lead to the degradation of SOFC performance [20,21]. The degradation of SOFC performance caused by Cr oxides is also known as "Cr poisoning". The degradation mechanism of electrolyte is mainly the reduction of YSZ intrinsic conductivity [22]. The degradation of interconnect is attributed to the decrease of electrical conductivity caused by the thin oxide layer formed on the surface [23]. For stainless steel materials, the oxide layer is mainly Cr_2O_3. The last type is anode material degradation, which mainly includes Ni particle coarsening, carbon deposition and impurity gas poisoning. Among the four types of material degradation, the degradation of anode materials is the most concerned, especially carbon deposition and Ni particle coarsening, because the materials degradation in other positions can be easily inhibited or even eliminated by external measures. For example, the formation of Cr_2O_3 in cathode and interconnect can be inhibited by adding an antioxidant layer on the surface of the metal interconnect plate [24]. The decrease of intrinsic conductivity of electrolyte YSZ is obvious at high temperature (above 1000 ^oC), but this decline is weakened at moderate temperature (600-800 ^oC).

However, Ni particle growth and carbon deposition are inherent degradation mechanisms, which are difficult to suppress through external measures and are unavoidable in operation. Carbon deposition is a typical problem that causes the performance degradation of SOFCs fueled by carbon hydrocarbons. The main reason is that the decomposition of the carbon-containing fuel produces solid carbon in the porous anode, resulting in the blockage of the anode pores, which blocks the active site of the reaction and makes the gas transport difficult. As a result, the reaction activity is reduced [25]. It is noteworthy

that there have been related reports on the carbon deposition phenomenon from the perspective of experiments and simulations [25–28]. It was summarized that the operating conditions can suppress the carbon deposition phenomenon. Ni coarsening is a problem that affects the durability of SOFC fed by all kind of fuels, which is also the main focus of this article. According to the current research, there are two different mechanisms to explain Ni particle growth: atomic migration and vapor transport [29]. Atomic migration means that Ni atoms escape from the small crystals and are trapped by the large crystals, encouraging the growth of Ni particles. Vapor transfer is a process that the Ni atoms at the edge site react with the kinked Ni atoms in the presence of steam to form the composite Ni_2-OH [29,30]. The specific process can be described by reaction equation (1). Under the humidified environment, the vapor transfer mechanism is generally viewed as the main reason of Ni coarsening [29]. In this work, the Ni particle growth model based on vapor transfer mechanism was used to describe Ni coarsening growth in SOFC anode.

$$2_{*\mathrm{Ni}(111)} + \mathrm{H_2O(g)} + 2\,\mathrm{Ni_{bulk}} \rightleftarrows \mathrm{Ni_2\text{-}OH}(2_{*\mathrm{Ni}(111)}) + 0.5\,\mathrm{H_2(g)} \quad (1)$$

There have been several reports on the influence mechanism and quantitative analysis of Ni coarsening on SOFC performance. Zhu et al. [31] established a two-dimensional humidified hydrogen fueled SOFC model coupled with Ni coarsening, and discussed the effect of the ratio of the initial Ni particle radius to the YSZ particle radius on the current density attenuation rate. Fu et al. [29] developed a three-dimensional multi-physics SOFC model coupled with Ni particle coarsening and quantified the voltage attenuation rate under different operating conditions. The fuel used in this SOFC model is a mixture of steam, methane and hydrogen. The solution time of the model is about 12-16 h. Such a long solution time is detrimental to real-time prediction of SOFC performance degradation and fast performance optimization. Rizvandi et al. [32] developed a multiscale degradation model of the SOFC stack fueled by humidified hydrogen, taking Ni coarsening, Cr poisoning, and interconnect plate oxidation into account. The solution time of this model in a high-end workstation is about 75 min. Through the analyses of the above studies, the previous work about Ni coarsening in SOFC fueled by biomass syngas is few, whose composition is more complex. Besides, the solution time of previous models is too long to meet the requirements of real-time prediction and fast optimization.

In this study, a multi-physics model of SOFC fueled by biomass syngas coupled with Ni particle coarsening is first developed. The relationship between microstructures and apparent performance of

porous electrode is quantified by using the binary random packing spherical particles model. Then the multi-physics field model is used to generate the adequate training data for the artificial neural network (ANN), which is used to predict the performance attenuation of SOFC caused by Ni coarsening. The multi-physics field (MPF) simulation can provide detailed information about SOFC performance attenuation under different operating and structural parameters, even under extreme conditions for training, which is difficult to achieve in experiment [33]. The ANN enables to quickly predict the performance attenuation based on the well-trained database generated by the MPF when the input parameters are given. The combination of ANN and MPF makes up for the lack of MPF in fast response. Furthermore, with the adoption of genetic algorithm (GA), the optimization of the SOFC regarding the objective function could be further achieved. Therefore, through the combination of MPF and ANN, rapid response prediction of SOFC performance attenuation under different conditions could be performed, so as to realize the fast optimization of SOFC performance. The proposed method contributes to significantly reduce the MPF computational load to a certain extent, and quickly screen out the optimal SOFC operation or structural parameters.

2. Model development

2.1 Research framework for combining transient MPF and ANN

Fig. 1 shows the framework of the proposed MPF and ANN combined model. The whole research framework can be divided into three parts. First, a transient multi-physics model of SOFC considering Ni particle coarsening is established, and then the model is validated to confirm its rationality. Then, the influences of relevant parameters on SOFC performance attenuation are investigated through the parametric analyses of the multi-physics model. If the influence mechanism of relevant parameters on SOFC performance attenuation is mastered, the indexes to characterize SOFC performance could be identified. After determining the independent variable parameters and dependent variable indexes, a large number of data sets are generated by running the MPF model. The independent variable parameters and dependent variable indexes are set as the inputs and outputs of the ANN, respectively. These data sets are divided into two parts: one for ANN to identify mappings between inputs and outputs, and the other for validating the accuracy of trained mature ANN. Finally, if the prediction accuracy of trained ANN meets the requirements, GA is used to optimize SOFC attenuation performance in a data-driven way to obtain the operating and structural parameters with practical

guiding significance. Through the combination of MPF, ANN, and GA, the real-time prediction and fast optimization of SOFC performance attenuation can be realized, which contributes to quickly screen out optimal parameters to improve SOFC durability under the influence of Ni coarsening.

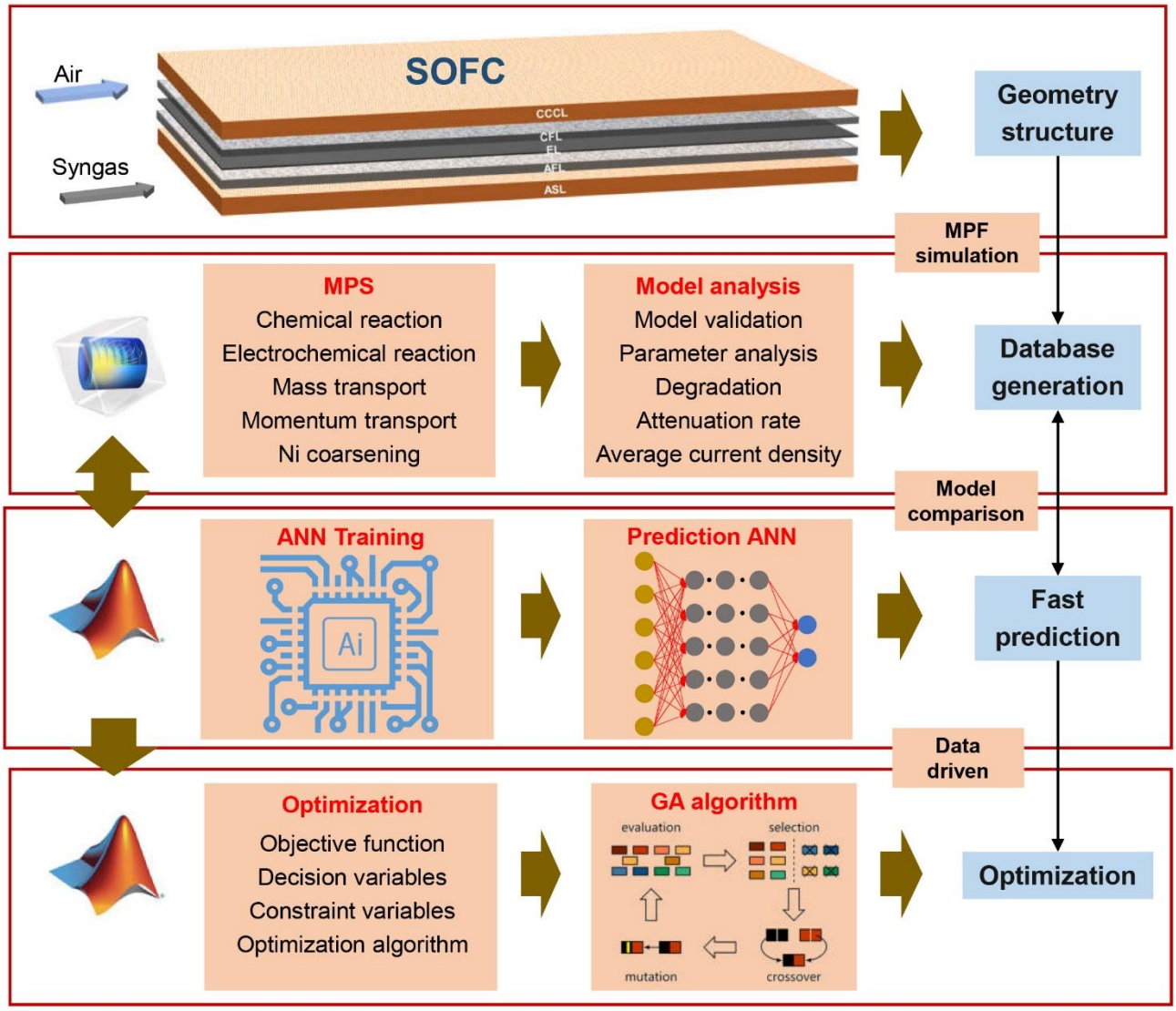


Fig. 1 The research framework for the developed MPF and ANN combined model

2.2 Geometric structure and working mechanism of SOFC

The two-dimensional geometric structure of the SOFC is shown in Fig. 2. The specific dimensional parameters, electrode and electrolyte parameters involved in this SOFC model are summarized in **Table 1**. In the developed model, the width of the single-channel cell is 2 mm and the area of the single-channel cell is 2 mm*4 cm=0.8 cm^2. The geometry of the model was also set according to the actual cell tested by Fu et al.[34]. As the actual cell consists of many single-channel cells, the single-channel cell is extracted for model construction to reduce the computational burden

based on the periodic geometry of the cell. The three-dimensional single-channel cell can be further simplified into two-dimensional single-channel cell when the interconnection plate is ignored [10]. The developed SOFC model is mainly composed of six components, which are anode and cathode flow channel, anode support layer (ASL), anode functional layer (AFL), electrolyte layer (EL), cathode functional layer (CFL) and cathode current collector layer (CCCL). The role of the flow channel is to provide a place for the circulation of fuel and air. The ASL is mainly used as a support to ensure the mechanical strength of the cell. The ASL is also the place where the reforming and shift reactions occur. AFL is filled with active sites where H_2 and CO react electrochemically with O^{2-} transported from the cathode [35]. The CFL provides the reaction sites where O^2 is oxidized to O^{2-} and conducts the O^{2-} to electrolyte region. The role of CCCL is relatively simple, which mainly collects the current.

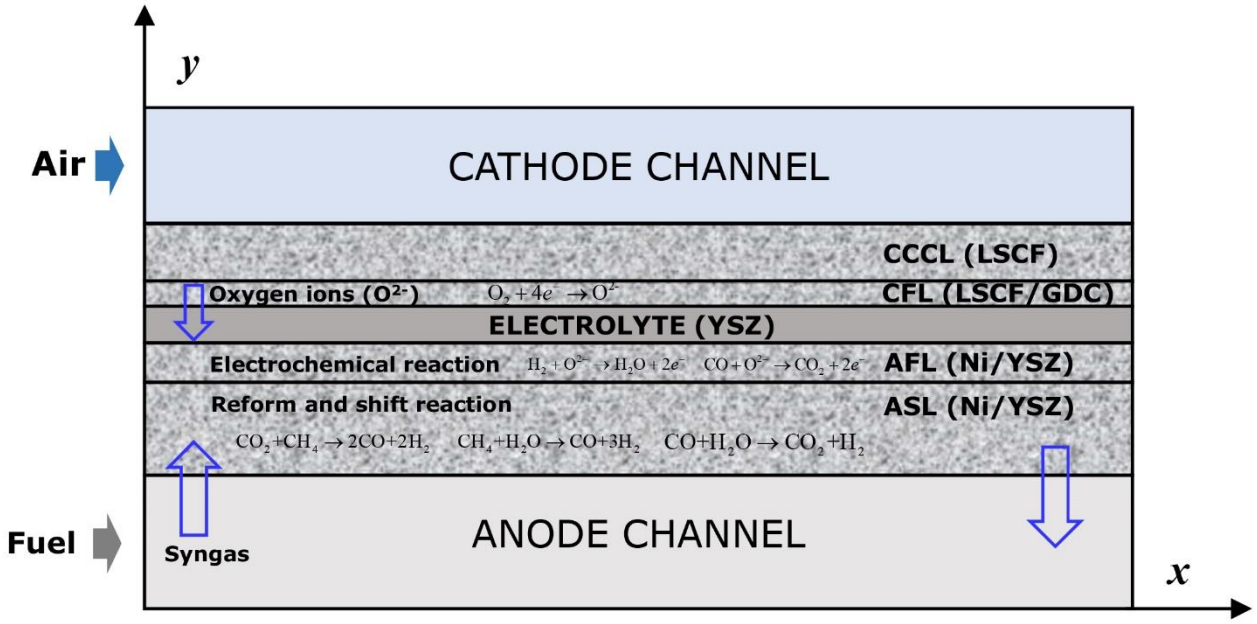


Fig. 2 The geometric structure of the SOFC (The schematic diagram of SOFC geometry was drawn with reference to the previous work [36]. The size of the SOFC shown in the figure is inconsistent with the actual size of the model. The specific SOFC model dimension can be found in **Table 1**)

Table 1 The main parameters involved in this MPF simulation model

Parameters	Value or expressions	Unit	Ref.
Geometric structure			
Cell length, L	40	mm	
Channel thickness, d_c	1	mm	

AFL thickness, d_{AFL}	0.01	mm	
ASL thickness, d_{ASL}	0.04	mm	
EL thickness, d_{EL}	0.015	mm	
CFL thickness, d_{CFL}	0.01	mm	
CCCL thickness, d_{CCCL}	0.02	mm	
Intrinsic electronic and ionic conductivity			
YSZ ionic conductivity, σ_{YSZ}	$3.34\times10^{4}\times e^{\frac{-10300}{T}}$	$S\cdot m^{-1}$	[9]
Ni electronic conductivity, σ_{Ni}	$3.27\times10^{6}-1065.3\times T$	$S\cdot m^{-1}$	[9]
GDC ionic conductivity, σ_{GDC}	$3.16\times10^{6}/T\times e^{\left(-5.33\times10^{4}/RT\right)}$	$S\cdot m^{-1}$	[37]
LSCF electronic conductivity, σ_{LSCF}	10000	$S\cdot m^{-1}$	[37]
AFL microscopic parameters			
AFL porosity, ε_{AFL}	0.3		[29]
Initial Ni particle diameter, d_{Ni0}	0.6	μm	[29]
YSZ particle diameter, d_{YSZ}	0.6	μm	[29]
AFL permeability, κ_{AFL}	2×10^{-11}	m^2	[34]
Ni phase volume fraction, ψ_{Ni}	0.4		
YSZ phase volume fraction, ψ_{YSZ}	0.6		
ASL microscopic parameters			
ASL porosity, ε_{AFL}	0.3		
Initial Ni particle diameter, d_{Ni0}	0.6	μm	[29]
YSZ particle diameter, d_{YSZ}	0.6	μm	[29]
ASL permeability, κ_{AFL}	2×10^{-10}	m^2	[34]
Ni phase volume fraction, ψ_{Ni}	0.4		
YSZ phase volume fraction, ψ_{YSZ}	0.5		
CFL microscopic parameters			
CFL porosity, ε_{CFL}	0.3		[29]

LSCF particle diameter, d_{LSCF}	0.5	μm	[29]
GDC particle diameter, d_{GDC}	0.5	μm	[29]
CFL permeability, κ_{CFL}	2×10^{-11}	m^2	[34]
LSCF phase volume fraction, ψ_{LSCF}	0.5		
GDC phase volume fraction, ψ_{GDC}	0.5		
CCCL microscopic parameters			
CCCL porosity, ε_{CCCL}	0.3		[29]
LSCF particle diameter, d_{LSCF}	0.5	μm	[29]
CCCL permeability, κ_{CCCL}	2×10^{-10}	m^2	[34]
LSCF phase volume fraction, ψ_{LSCF}	1		

2.3 MPF model for SOFC

The multi-physics field model mainly consists of chemical reaction, electrochemical reaction, mass transfer and momentum transfer. The governing equations of MPF model are discussed as follows based on the working principle of each region.

2.3.1. Model assumptions

- The fuel gas for the electrochemical reaction is only CO and H_2, because of the fast electrochemical reaction rates of CO and H_2 [10].
- The flow in the fuel and air channel is laminar due to the low Reynolds number of the flow in the channels.
- The cathode air is composed of 79% N_2 and 21% O_2.
- The SOFC is considered local isothermal due to the small cell size [38].
- The active sites of chemical and electrochemical reactions are uniformly distributed.
- The gases involved in the MPF model obey the ideal gas equation of state.

2.3.2. Chemical reaction model

Generally speaking, three types of reforming and shift reactions take place in ASL under the syngas atmosphere [39]. The first reaction is methane steam reforming (MSR) reaction, as show in Eq. (1). The second reaction is water gas shift (WGS) reaction, as show in Eq. (2). The last reaction is reverse methanation (RM) reaction, as shown in Eq. (3).

$$CH_4+H_2O \rightarrow CO+3H_2 \ \Delta H = 204 \text{ kJ/mol} \quad (1)$$

$$CO+H_2O \rightarrow CO_2+H_2 \ \Delta H = -41 \text{ kJ/mol} \quad (2)$$

$$CH_4+2H_2O \rightarrow CO_2+4H_2 \ \Delta H = 164 \text{ kJ/mol} \quad (3)$$

The corresponding reaction kinetics equations of the three reactions are shown in Eqs.(4)-(6) [35].

$$R_{\mathrm{I}} = \frac{\eta}{33480}\frac{k_1}{p_{\mathrm{H_2}}^{2.5}}\left(p_{\mathrm{CH_4}}p_{\mathrm{H_2O}} - \frac{p_{\mathrm{H_2}}^3 p_{\mathrm{CO}}}{K_{\mathrm{eq,I}}}\right)\Big/ DEN^2 \ \mathrm{mol}\cdot\mathrm{m_{cat}^{-2}}\cdot\mathrm{s^{-1}} \quad (4)$$

$$R_{\mathrm{II}} = \frac{\eta}{33480}\frac{k_2}{p_{\mathrm{H_2}}}\left(p_{\mathrm{CO}}p_{\mathrm{H_2O}} - \frac{p_{\mathrm{H_2}}p_{\mathrm{CO}}}{K_{\mathrm{eq,II}}}\right)\Big/ DEN^2 \ \mathrm{mol}\cdot\mathrm{m_{cat}^{-2}}\cdot\mathrm{s^{-1}} \quad (5)$$

$$R_{\mathrm{III}} = \frac{\eta}{33480}\frac{k_3}{p_{\mathrm{H_2}}}\left(p_{\mathrm{CH_4}}p_{\mathrm{H_2O}}^2 - \frac{p_{\mathrm{H_4}}^4 p_{\mathrm{CO_2}}}{K_{\mathrm{eq,III}}}\right)\Big/ DEN^2 \ \mathrm{mol}\cdot\mathrm{m_{cat}^{-2}}\cdot\mathrm{s^{-1}} \quad (6)$$

$$DEN = 1+K_{\mathrm{CO}}p_{\mathrm{CO}}+K_{\mathrm{H_2}}p_{\mathrm{H_2}}+K_{\mathrm{CH_4}}p_{\mathrm{CH_4}}+K_{\mathrm{H_2O}}\frac{p_{\mathrm{H_2O}}}{p_{\mathrm{H_2}}} \quad (7)$$

where k represents the reaction rate constant; K_{eq} represents the reaction equilibrium constant; p represents the partial pressure; K represents the adsorption constant; η is the effectiveness factor, which is assumed as 0.03 [40].

2.3.3. Electrochemical reaction model

The half-electrode reactions at the anode and the half-electrode reaction at the cathode are shown in Eqs. (8)-(10).

$$\text{Anode: } H_2+O^{2-} = H_2O + 2e^- \quad (8)$$

$$\text{Anode: } CO+O^{2-} = CO_2 + 2e^- \quad (9)$$

$$\text{Cathode: } O_2=2O^{2-} - 4e^- \quad (10)$$

The electrochemical reaction kinetics is determined by the Butler-Volmer formula, which is described as Eq. (11).

$$i = i_0\left\{\frac{C_{\mathrm{R}}}{C_{\mathrm{R,ref}}}\exp\left(\frac{\alpha n F \eta_{\mathrm{act}}}{RT}\right) - \frac{C_{\mathrm{O}}}{C_{\mathrm{O,ref}}}\exp\left(\frac{-(1-\alpha)nF\eta_{\mathrm{act}}}{RT}\right)\right\} \quad (11)$$

where i represents the electrode current density; i_0 represents the exchange current density, which is calculated by Eq. (12); α represents the charge transfer diffusion coefficient; n represents the number

of electrons transferred in the electrochemical reaction; F represents the Faraday constant; R represents the ideal gas constant; T represents the temperature; η_{act} represents the activation over potential; C_R and C_O are the reduction and the oxide concentration, respectively; $C_{R,ref}$ and $C_{O,ref}$ are the reduction and the oxide reference concentration, respectively.

$$i_0 = \gamma \frac{RT}{nF} \exp\left(\frac{-E_{act}}{RT}\right) \tag{12}$$

where γ is the pre-exponential factor; E_{act} is the activation energy; γ is pre-exponential factor. The activation energy is 100 kJ·mo1^{-1} for anode and 120 kJ·mo1^{-1} for cathode [41]. The pre-exponential factor is 5×10^9 S·m^{-2} for anode and 2×10^9 S·m^{-2} for cathode [41].

The volume current density of electrode is calculated by Eq. (13).

$$j = i \cdot \lambda_{TPB} \tag{13}$$

where λ is the triple phase boundary (TPB) area per unit volume

The relationship between the equilibrium potential E_{eq} and the output voltage V can be referred to our previous work [9].

2.3.4. Mass transfer model

The mass transfer governing equations are discussed in two cases, one is the mass transfer in the flow channel, and the other is the mass transfer in the porous electrode. The mass transport process in the flow channel belongs to the mass transfer without any filling medium, which can be described by Eq. (13). The electrode region is filled with porous media, so the influence of porous media should be taken into account in the mass transfer governing equation inside the electrode region. The governing equation in the electrode region is shown in Eq. (14). It is worth noting that the transient model is established in this paper, so the unsteady term is considered in the mass transfer equations of both electrode and flow channel regions. Moreover, due to the presence of electrochemical or chemical reactions in the electrode region, the source term in the governing equation is generated.

$$\rho \frac{\partial \omega_i}{\partial t} + \nabla \cdot \boldsymbol{j}_i + \rho(\boldsymbol{u} \cdot \nabla)\omega_i = 0 \tag{13}$$

$$\varepsilon\rho \frac{\partial \omega_i}{\partial t} + \nabla \cdot \boldsymbol{j}_i + \rho(\boldsymbol{u} \cdot \nabla)\omega_i = R_i \tag{14}$$

$$\boldsymbol{j}_i = -\left(\rho D_i^m \nabla \omega_i + \rho \omega_i D_i^m \frac{\nabla M_n}{M_n} - \rho \omega_i \sum_k \frac{M_i}{M_n} D_k^m \nabla x_k\right) \tag{15}$$

where ρ is the density of gas mixture; ω_i is the mass fraction of species i; $\boldsymbol{j}_i$ is the mass diffusion flux of species i; $\boldsymbol{u}$ is the velocity of the gas mixture; ε is the porosity of electrode; R_i is the rate of generation or consumption of species i; M_i is the molar mass of species i; x_k is molar fraction of species k; D_i^m is mean diffusion coefficient of species i, which is calculated by Eq. (16); M_n is mean molar mass, which is calculated by Eq. (17).

$$D_i^m = \frac{1-\omega_i}{\sum_{k\neq i}\frac{x_k}{D_{ik}}} \tag{16}$$

$$M_n = \left(\sum_i \frac{\omega_i}{M_i}\right)^{-1} \tag{17}$$

where D_{ik} is the binary diffusion coefficient between species i and species k, whose definition could be found in our previous work [9]. In the porous media region, the binary diffusion coefficient needs to be modified to the effective binary diffusion coefficient. The specific correction method can also refer to our previous work.

2.3.5. Momentum transfer model

Similar to mass transfer model, momentum transfer governing equation has two different expressions. In the flow channel, it is the classical unsteady N-S equation and mass conservation equation, as shown in Eqs. (18) and (19). In the porous electrode, it is the N-S equation that considers Darcy's seepage, as shown in Eq. (20), also named Brinkman equation. The mass conservation in porous medium is shown as Eq. (21).

$$\rho\frac{\partial \boldsymbol{u}}{\partial t} + \rho\left(\boldsymbol{u}\cdot\nabla\right)\boldsymbol{u} = -\nabla p + \nabla\cdot\left[\mu\left(\nabla\boldsymbol{u} + \left(\nabla\boldsymbol{u}\right)^{\mathrm{T}}\right) - \frac{2}{3}\mu\left(\nabla\cdot\boldsymbol{u}\right)\boldsymbol{I}\right] \tag{18}$$

$$\frac{\partial \rho}{\partial t} + \nabla\cdot\left(\rho\boldsymbol{u}\right) = 0 \tag{19}$$

$$\frac{\rho}{\varepsilon}\frac{\partial \boldsymbol{u}}{\partial t} + \rho\left(\boldsymbol{u}\cdot\nabla\right)\boldsymbol{u} = \nabla\cdot\left[-p\boldsymbol{I} + \frac{\mu}{\varepsilon}\left(\nabla\boldsymbol{u} + \left(\nabla\boldsymbol{u}\right)^{\mathrm{T}}\right) - \frac{2}{3}\frac{\mu}{\varepsilon}\left(\nabla\cdot\boldsymbol{u}\right)\boldsymbol{I}\right] - \left(\frac{\mu}{\kappa} + \frac{Q_{\mathrm{m}}}{\varepsilon^2}\right)\boldsymbol{u} \tag{20}$$

$$\frac{\partial (\varepsilon\rho)}{\partial t} + \nabla\cdot\left(\rho\boldsymbol{u}\right) = Q_{\mathrm{m}} \tag{21}$$

where $\boldsymbol{u}$ is velocity vector; ρ is the density of the fluid; p is pressure; μ is dynamic viscosity of the gas mixture; $\boldsymbol{I}$ is unit matrix; κ is permeability of the porous media; ε is porosity of the porous media; Q_{m}

is mass source term caused by chemical and electrochemical reactions. The calculation method of the dynamic viscosity of the gas mixture could be also found in Ref. [9].

2.4 Ni coarsening model for SOFC

In this work, the vapor transport mechanism is used to describe the growth process of Ni particles in SOFC anode. Based on the vapor transport mechanism, Sehested et al. [30] proposed the sintering model of Ni based catalyst to describe the increase of Ni particle diameter. Fu et al. [29] determined the constants in the model by fitting experimental data. Finally, the Ni particle growth model is described by Eq. (22).

$$d_t = \left[\alpha \frac{\psi_{\mathrm{Ni}}}{(1-\psi_{\mathrm{Ni}}) A_{\mathrm{io}}} \left(\frac{p_{\mathrm{H_2O}}}{p_{\mathrm{H_2}}^{0.5}} \right) \exp\left(\frac{-E_a}{RT} \right) t + d_0^n \right]^{1/n} \tag{22}$$

where d_t is the diameter of Ni particle at time t; ψ_{Ni} is Ni phase fraction; A_{io} is specific surface area of electrolyte skeleton in anode (μm^{-1}); $p_{\mathrm{H_2O}}$ and $p_{\mathrm{H_2}}$ are steam and hydrogen partial pressure (bar), respectively; E_a is the total energy barrier (242 $kJ \cdot mol^{-1}$); d_0^n is the initial Ni particle diameter (μm); n is characteristic exponent related to the transport mechanism, which is 8 according to the fitting result; α is the pre-exponential factor (3.04×10^8 $\mu m^{n-1} bar^{-0.5} h^{-1}$).

2.5 Microscopic binary random filled sphere model

The binary random filled sphere (BRFS) model is a bridge between the microstructure and macroscopic performance characteristics of the cell. In BRFS model, Ni particles, YSZ particles, GDC particles and LSCF particles are regarded as regular spherical particles. Through the BRFS model, parameters such as the three-phase interface area of the electrode and the specific surface area of Ni particles can be obtained. As a result, the changes of electrode microstructure will be mapped to the macro performance of the cell. Although it is an idealized assumption to treat electrode particles as regular spheres, it gives a possibility to communicate microstructure and macroscopic performance. Furthermore, the BRFS model has also been widely used in the past decades. Therefore, the BRFS model is also developed here to discuss the influence of Ni particle growth on the macroscopic performance of the cell. The BRFS model is described as follows.

2.5.1 Micro model

The SOFC electrodes mainly contain three kinds of particles, which are electronic conductive phase, ionic conductive phase and mixed conductive phase. In this SOFC model, Ni particles are electronic conductive phase, while GDC and YSZ particles are ionic conductive phase. LSCF particles are mixed conductive phase. According to BRFS theory, the coordination number, percolation probability, total particle number and some microscopic parameters could be calculated. Note that in the following Eqs. (23)-(26), the subscript "el" represents the electron conducting phase and the subscript "io" represents the ionic conducting phase. In addition, with the coarsening of Ni particles, the radius of Ni particles varies with time. However, the melting point of YSZ is high, so the skeleton formed by YSZ is almost unchanged. That's to say, the radius of YSZ particles keeps unchanged [42].

$$Z_{\text{el-el}} = Z \cdot \frac{\psi_{\text{el}} / r_{\text{el}}}{\psi_{\text{el}} / r_{\text{el}} + \psi_{\text{io}} / r_{\text{io}}} \tag{23}$$

$$Z_{\text{io-io}} = Z \cdot \frac{\psi_{\text{io}} / r_{\text{io}}}{\psi_{\text{el}} / r_{\text{el}} + \psi_{\text{io}} / r_{\text{io}}} \tag{24}$$

$$Z_{\text{el-io}} = \frac{Z}{2} \cdot \left(1 + \frac{r_{\text{el}}^2}{r_{\text{io}}^2}\right) \cdot \frac{\psi_{\text{io}} / r_{\text{io}}}{\psi_{\text{el}} / r_{\text{el}} + \psi_{\text{io}} / r_{\text{io}}} \tag{25}$$

$$Z_{\text{io-el}} = \frac{Z}{2} \cdot \left(1 + \frac{r_{\text{io}}^2}{r_{\text{el}}^2}\right) \cdot \frac{\psi_{\text{el}} / r_{\text{el}}}{\psi_{\text{el}} / r_{\text{el}} + \psi_{\text{io}} / r_{\text{io}}} \tag{26}$$

where $Z_{\text{el-el}}$, $Z_{\text{io-io}}$, $Z_{\text{el-io}}$, $Z_{\text{io-el}}$ are coordination number between electron conducting phase and electron conducting phase, ion conducting phase and ion conducting phase, electron conducting phase and ion conducting phase, ion conducting phase and electron conducting phase, respectively; Z is the average coordination number, which is assumed as 6 [43]; r is the particle radius; ψ is the volume fraction of particles.

The percolation probability refers to the probability that particles form percolation clusters, and thus forming the conductive paths in the whole electrode [43]. It can be divided into electron percolation probability and ion percolation probability according to different electrode conduction types. The percolation probability can be calculated by Eqs. (27) and (28) [43].

$$P_{\text{el}} = \left(1 - \left(\frac{3.764 - Z_{\text{el-el}}}{2}\right)^{2.5}\right)^{0.4} \tag{27}$$

$$P_{\mathrm{io}}=\left(1-\left(\frac{3.764-Z_{\mathrm{io\text{-}io}}}{2}\right)^{2.5}\right)^{0.4} \tag{28}$$

where P represents percolation probability.

The number of total particles per unit volume of the electrode can be calculated by Eq. (29) [43], where ξ_{el} and ξ_{io} represent the ratio of the number of particles in the electronic or ionic conductive phase to the total number of particle, respectively.

$$N=\frac{1-\varepsilon}{4/3\pi r_{\mathrm{el}}^3\xi_{\mathrm{el}}+4/3\pi r_{\mathrm{el}}^3\xi_{\mathrm{el}}} \tag{29}$$

$$\xi_{\mathrm{el}}=\frac{\psi_{\mathrm{el}}/r_{\mathrm{el}}^3}{\psi_{\mathrm{el}}/r_{\mathrm{el}}^3+\psi_{\mathrm{io}}/r_{\mathrm{io}}^3} \tag{30}$$

$$\xi_{\mathrm{io}}=\frac{\psi_{\mathrm{io}}/r_{\mathrm{io}}^3}{\psi_{\mathrm{el}}/r_{\mathrm{el}}^3+\psi_{\mathrm{io}}/r_{\mathrm{io}}^3} \tag{31}$$

where; N is the total number of particles; ε is the porosity.

2.5.2 Triple phase boundary area model

The TPB refers to an interface between electronic conductive particles, ionic conductive particles and pores, which could transfer electrons, ions and gas molecules simultaneously. Specifically, the TPB in the SOFC anode refers to the interface of Ni-YSZ-pore. Because the junction of Ni-YSZ-pore is a line actually, also known as TPB line. Since the TPB line is difficult to support electrochemical reactions, the TPB line is generally extended to the surface of particles of limited width near the TPB line, shown in dashed region of Fig. 3. According to BSFC theory, anode TPB area can be obtained by calculating the area at the junction of Ni-YSZ-pore, as shown in Eq. (32).

$$\lambda_{\mathrm{an}}=2\pi\min\left(r_{\mathrm{el}},r_{\mathrm{io}}\right)\sin\theta\cdot w\cdot N\xi_{\mathrm{el}}Z_{\mathrm{el\text{-}io}}P_{\mathrm{el}}P_{\mathrm{io}} \tag{32}$$

where θ is the contact angle, which is assumed as 15°; w is the active width of the contact line, which is set as 20 nm [44].

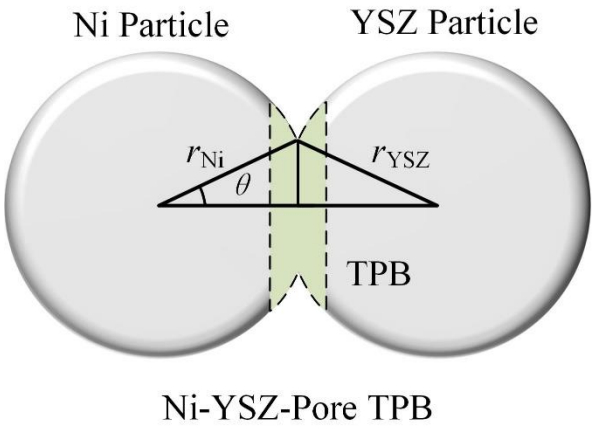


Fig. 3 Schematic diagram of the three phase boundary

As the LSCF is the mixed conductive phase, so the TPB of the cathode could be simplified into the double phase boundary (DPB), i.e. LSCF-pore interface. The DPB area per unit volume of the cathode only needs to calculate the surface area of the LSCF particles exposed in the pore, as expressed in Eq. (33). It is worth noting that LSCF is still treated as electron conductivity phase when calculating the coordination number, percolation probability and other microscopic parameters.

$$\lambda_{ca} = 2\pi r_M^2 \left(2 - \left(1-\cos\theta\right)\cdot Z_{el\text{-}el} - \left(1-\cos\theta\right)\cdot Z_{el\text{-}io}\right)\cdot N\xi_{el}P_{el}P_{io} \tag{33}$$

where r_M represents the radius of LSCF particles. Because both LSCF and GDC can conduct O^{2-}, P_{io} is set to 1.

2.5.3 The specific surface area model

Since the Ni particles in the ASL region also act as catalysts for chemical reactions, the specific surface area per unit volume of Ni particles is calculated to obtain the reaction rate. The specific surface area of Ni particles is calculated by Eq. (34).

$$A_{Ni} = 2\pi r_{Ni}^2 \left(2 - \left(1-\cos\theta\right)\cdot Z_{el\text{-}el} - \left(1-\cos\theta\right)\cdot Z_{el\text{-}io}\right)\cdot N\xi_{el} \tag{34}$$

where A_{Ni} is the specific surface area of Ni particles; r_{Ni} is the radius of Ni particles.

The growth of Ni particles will be hindered by YSZ skeleton. The specific surface area of YSZ particles is calculated by Eq. (35).

$$A_{io} = 2\pi r_{io}^2 \left(2 - \left(1-\cos\theta\right)\cdot Z_{io\text{-}io} - \left(1-\cos\theta\right)\cdot Z_{io\text{-}el}\right)\cdot N\xi_{io} \tag{35}$$

2.5.4 The effect conductivity model

The growth of Ni particles also has an impact on the conductivity of the particles, which is realized by Eqs. (36) and (37) [45].

$$\sigma_i^{\mathrm{el,eff}} = \sigma_i^{\mathrm{el},0}\left((1-\varepsilon)\psi_i P_{\mathrm{el}}\right)^{\gamma} \tag{36}$$

$$\sigma_j^{\mathrm{io,eff}} = \sigma_j^{\mathrm{io},0}\left((1-\varepsilon)\psi_j P_{\mathrm{io}}\right)^{\gamma} \tag{37}$$

where $\sigma_i^{\mathrm{el,eff}}$ is the effective electronic conductivity of phase *i*; $\sigma_i^{\mathrm{el},0}$ is the intrinsic electronic conductivity of phase *i*; $\sigma_j^{\mathrm{io,eff}}$ is the effective ionic conductivity of phase *j*; $\sigma_j^{\mathrm{io},0}$ is the intrinsic ionic conductivity of phase *j*; γ is the Bruggeman factor, which is assumed as 1.5 [45].

The parameters involved in the BRFS model, such as phase fraction, particle diameter, etc., are listed in **Table 1**.

2.6 The performance attenuation indexes

To clearly evaluate the performance of SOFC under the influence of Ni particle coarsening, the MPF model simulates the evolution of SOFC performance over 20,000 hours in this work. The attenuation rate per thousand hours and average current density are defined here to characterize the performance attenuation of SOFC. The definitions of attenuation rate per thousand hours (r) and average current density ($\bar{I}$) are is shown in Eqs. (38) and (39), respectively.

$$r = \frac{I_{20\mathrm{K}} - I_0}{20} \times 100\% \tag{38}$$

$$\bar{I} = \frac{\int_0^{20\mathrm{K}} I(t)\,dt}{20\mathrm{K}} \tag{39}$$

where I_0 is the initial current density; $I_{20\mathrm{K}}$ is current density at 20 kh (20,000 hours).

2.7 Validation of MPF simulation for SOFC

The model developed in this work can be divided into two parts, one is the MPF model and the other is the BRFS model. The BRFS model is established by considering electrode particles as ideal spheres, which is a kind of idealized model to some extent. Although the BRFS model is a microscopic description of electrode particles, which is difficult to be validated by experiments, it has been widely accepted as a bridge between the macroscopic performance and microstructure of electrodes [31,43]. Therefore, the MPF model is just validated in this work. The SOFC generally have two opposite operating modes, which are electricity generation mode and electrolysis mode. In electric mode, the cell is charged by fuel gas to generate electricity; while in electrolytic mode, which is also called SOEC (Solid oxide electrolytic cell), the cell is powered by electricity to generate hydrogen from water. In

this work, the discharge mode of SOFC is only focused on, so the polarization curve of SOFC discharge process is validated. The SOEC's model is not investigated in current work and could not validate it. However, the SOEC model has been reported and validated in other reported work [46,47]. In the validation process, all parameters settings are consistent with Ref. [34]. The details of the parameters used for model validation and process can be found in the supporting materials. In order to make up for the difference of simplifying 3D to 2D, the charge transfer diffusion coefficient α is adopted as the tuning parameter to debug the validation model. It can be seen from Fig. 4 that the experimental data are in good agreement with the simulation results, thus confirming the reliability of the MPF model.

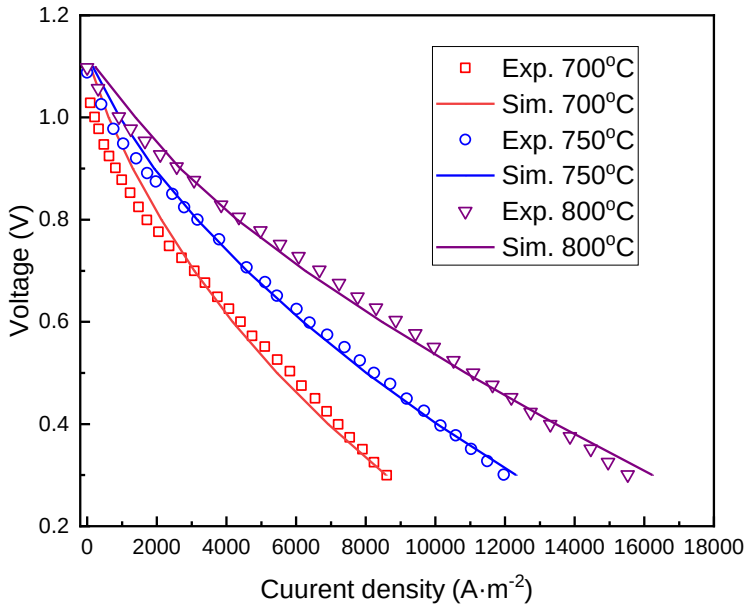


Fig. 4 The comparison of experimental and MPF *I-V* characteristics

2.8 Combination of MPF model with ANN prediction

Although the MPF model could analyze the performance of SOFC, MPF simulation needs to couple many physical fields and the simulation is too complex, resulting in a long calculation time. Therefore, it is necessary to develop a fast prediction method for SOFC attenuation performance. Compared with MPF model, ANN could map input variables to output variables quickly and accurately, especially for highly nonlinear models. Combining the MPF model and the ANN algorithm will greatly improve the speed and accuracy of predicting the SOFC attenuation performance. The MPF model is mainly used to generate a large number of databases for training ANN, which is to establish nonlinear

function relations between inputs and outputs. Furthermore, compared with the experimental test to capture a large amount of data, the MPF could save expensive costs and time.

The MPF generates more than 800 data samples. Each data sample includes 6 input variables and 2 output variables. The input variables include temperature, initial Ni particle diameter and other operating and structural parameters that have important impacts on SOFC attenuation performance. The output variables are selected to evaluate the SOFC attenuation performance as defined above: thousand hours' attenuation rate and average output current density. In other words, the MPF will produce an 819×8 data matrix as a training data set. The data set will be randomly divided into two parts based on the ratio of 9:1, with 90% of the data for ANN training and 10% for testing. Based on these data samples, a 6×5×2 ANN is constructed, as shown in Fig. 5. The epoch is set as 200 and the training goal is set as 4E-5.

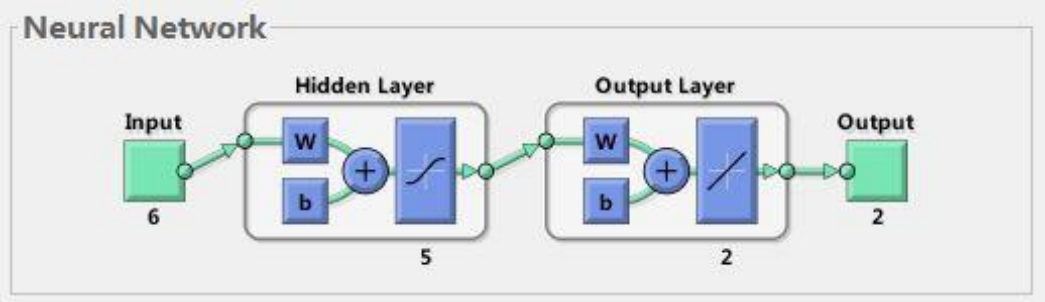


Fig. 5 The schematic of the constructed ANN

On the basis of training mature ANN models, a data-driven approach is adopted to optimize SOFC performance. In other words, the mature ANN is used as a mapping function between inputs and outputs, and GA algorithm is used to optimize the objective functions. As a source heuristic optimization algorithm, GA is particularly suitable for optimization problems without definite function relations in practical applications. Moreover, GA has also been widely used in practical applications currently. In this practical problem, the genetic algebra is 100, the population size is 60, the crossover probability is 0.4, and the mutation probability is 0.2.

3. Results and discussion

First, the influences of related operating parameters and structural parameters on SOFC performance attenuation are discussed and analyzed. Then, the appropriate operating parameters and structural parameters which significantly determine the attenuation of cell performance, are selected as the input variables to train ANN. The selected operating parameters are operating temperature,

potential and fuel composition. The selected structural parameters are initial Ni particle diameter, YSZ particle diameter, Ni phase volume fraction and anode porosity. The detailed information about the selected parameters is listed in **Table 2**. The single parameter is investigated here, which means that when one of the parameters is investigated, the other parameters keep the typical values. The typical anode inlet molar fuel composition is y_{H_2}: y_{CO}: y_{CO_2}: y_{CH_4}: y_{H_2O}=0.4: 0.2: 0.1: 0.1: 0.2.

Table 2 Parameters and value ranges for parameter analysis and ANN input variables

Parameters	Typical value	Value range	Unit
Operating temperature	750	650-810	ºC
Operating potential	0.6	0.3-0.8	V
Initial Ni particle diameter	0.6	0.5-0.7	μm
YSZ particle diameter	0.6	0.5-0.7	μm
Ni phase volume fraction	0.4	0.35-0.55	-
Anode porosity	0.3	0.25-0.50	-
Anode fuel velocity	0.5	-	$m \cdot s^{-1}$
Cathode air velocity	1.0	-	$m \cdot s^{-1}$

3.1 The effect of operating temperature

The influence of temperature on SOFC transient performance is shown in Fig. 6. As the temperature increases, the Ni particle diameter increases to a larger extent. As can be seen from the formula of Ni particle coarsening, Ni particle diameter gradually increases with the increase of temperature. It can be seen from Fig. 6(a), when the temperature is 650 ºC, the Ni particle diameter increases to 0.63 μm at 2 kh, while the Ni particle diameter increases to 0.945 μm at 2 kh at the elevated temperature of 800 ºC. The effect of the increased Ni particle diameter is that the percolation probability of electron conductive phase P_{el} and the TPB area decrease, as shown in Fig. 6(b) and Fig. 6(c). Furthermore, the higher the temperature is, the larger the Ni particle diameters are, and the faster the decrease of TPB and percolation probability is. For example, when the temperature is 650 ºC, the percolation probability decreases from 0.82 to 0.80 and TPB area from 71581 m^{-1} to 64399 m^{-1}. By comparison, when the temperature is 800 ºC, the percolation probability decreases from 0.82 to 0.23 and TPB area from 71581 m^{-1} to 10433 m^{-1}. In particular, the percolation probability of electron conductive phase is

reduced by 0.23 in 20 kh at 800 ºC. This means that the connectivity of the electronic conductive phase is already poor, and the cell performance attenuation should be very severe. The characterization of the effect of temperature on SOFC performance is reflected on the current density. As can be seen from Fig. 6(d), the higher the temperature is, the higher the current density as a whole in the entire calculation life cycle is, but the larger the attenuation rate is. For example, when the temperature is 800 ºC, the current density is higher than that at 650 ºC throughout the computational life cycle. But the attenuation rate of current density is 2.6%/kh at 800 ºC, which is also larger than that corresponding to 650 ºC (0.23%/kh). This is mainly because the higher temperature results in the faster electrochemical reaction rate and the larger overall corresponding current density. On the other hand, the higher temperature also brings about more obvious Ni particles coarsening and the greater current density attenuation as a result. This is also why the average current density and attenuation rate are used to evaluate SOFC attenuation performance in this work. In order to limit the attenuation rate within a certain range and ensure a higher average current density, it is recommended that SOFC operates at 750 ºC according to Fig 6(d). When SOFC is operated at 750 ºC, the current density attenuation rate is 1.5%/kh and the average current density is 5214 $A \cdot m^{-2}$. Although the current density attenuation rate does not meet the requirement of 1%/kh, it can be further reduced by optimizing other parameters. If the operating temperature is further reduced, the average current density will be even lower.

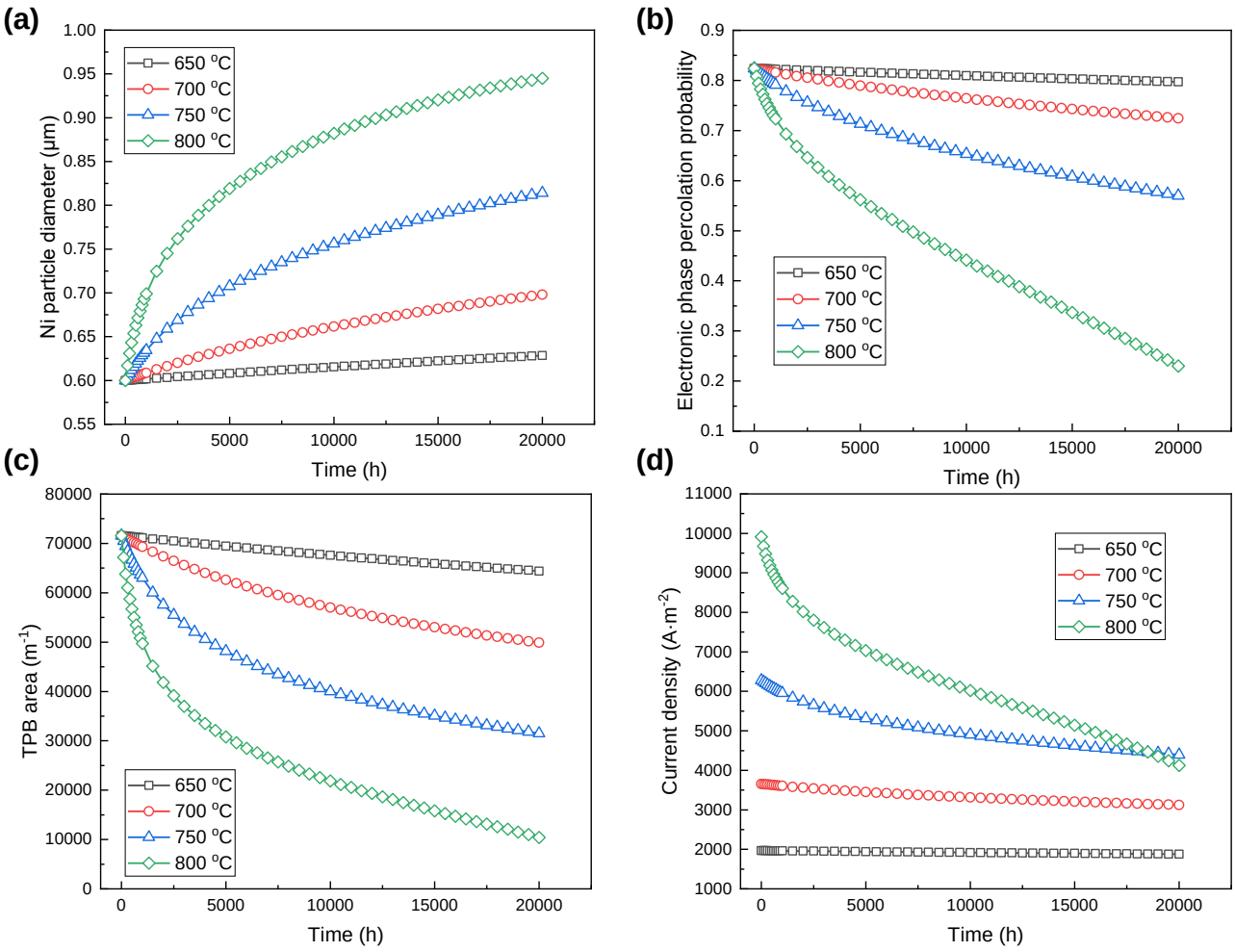


Fig. 6 The effect of operating temperature on (a) Ni particle diameter; (b) electronic conductive phase percolation probability; (c) effective area of TPB; (d) current density.

Fig. 7 shows the spatial distribution of intermediate variables at t=10 kh. It can be seen that the distribution of partial pressure ratio $p_{H_2O} / p_{H_2}^{0.5}$ is consistent with the distribution of Ni particle diameter. However, the spatial distribution of Ni particle diameter is opposite to the spatial distribution of percolation probability and TPB area. This can be confirmed by the corresponding formulas as shown in Eq. (22), Eq. (27) and Eq. (32). This is also consistent with the information shown in Fig. 6 about the distribution of variables over time. The coincidence of time and space also reflects the rationality and correctness of the solution.

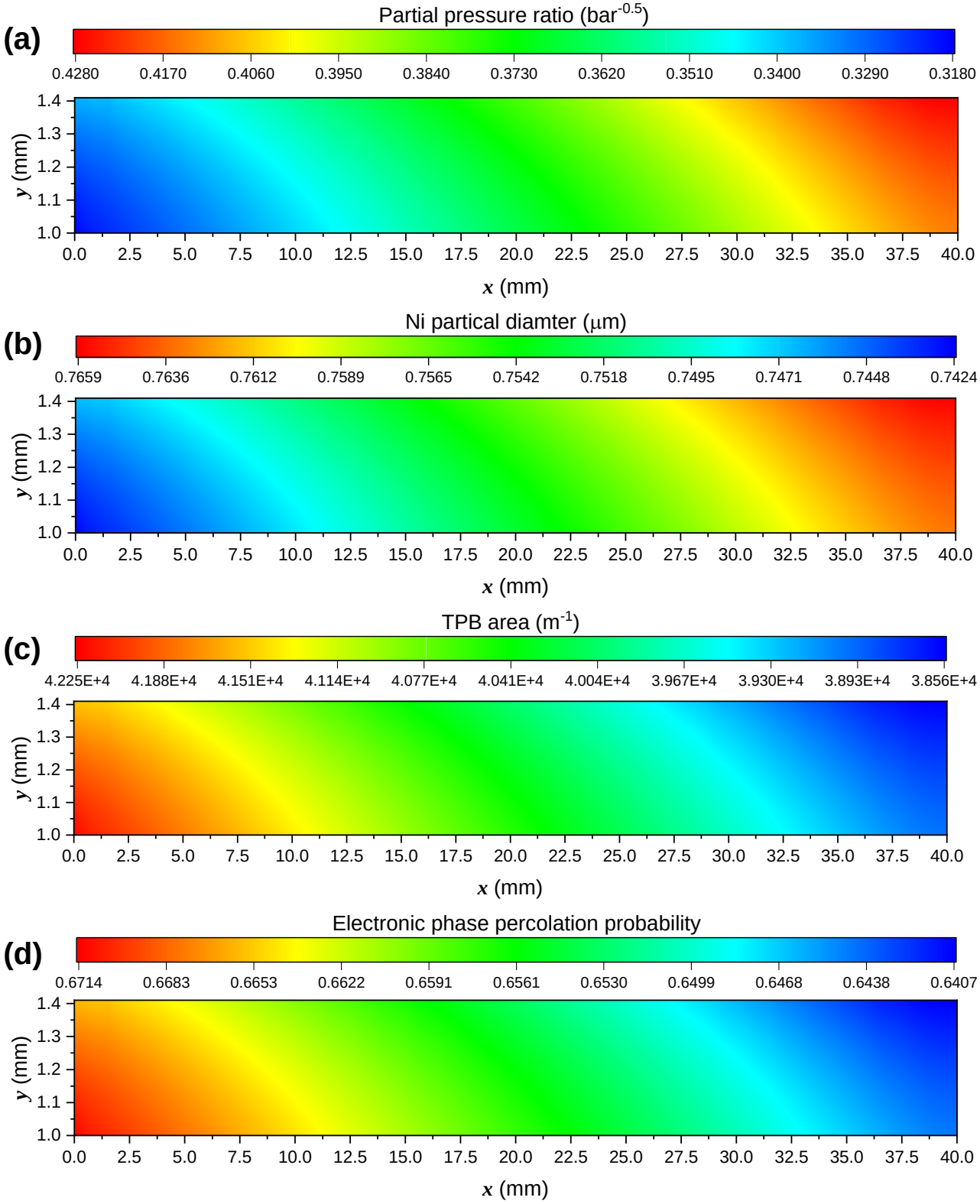


Fig. 7 The spatial distribution at t=10 kh and 750 ºC of (a) partial pressure; (b) Ni particle diameter; (c) TPB effective area; (d) electronic conductivity phase percolation probability.

3.2 The effect of operating voltage

The influence of operating voltage on SOFC transient performance is relatively simple, which affects the coarsening of Ni particles by adjusting the partial pressure ratio inside the SOFC anode. The improvement in operating voltage means a decrease in current density. Therefore, the amount of hydrogen involved in the electrochemical reaction decreases. The partial pressure of residual hydrogen increases and the partial pressure of steam decreases inside the anode. As a result, the partial pressure ratio $p_{H_2O} / p_{H_2}^{0.5}$ shown in Fig. 7(b), reduces with the increase of operating voltage. Accordingly, the decrease of Ni particle coarsening and TPB areas slows down, as shown in Fig. 7(a) and Fig. 7 (c). The characterization performance directly reflected on SOFC is the reduction of attenuation rate. It can be seen from Fig. 7(d), the attenuation rate of SOFC current density decreases from 1.565%/kh to 1.355%/kh as the operating voltage gradually increases. It should be noted that the suppression of cell attenuation by increasing voltage is relatively limited. Moreover, raising the voltage too much will significantly reduce the average current density and deviate from the ideal cell operating point. Therefore, it is generally recommended that the voltage should be maintained within the appropriate range. The selected operating voltage here is typically 0.6 V.

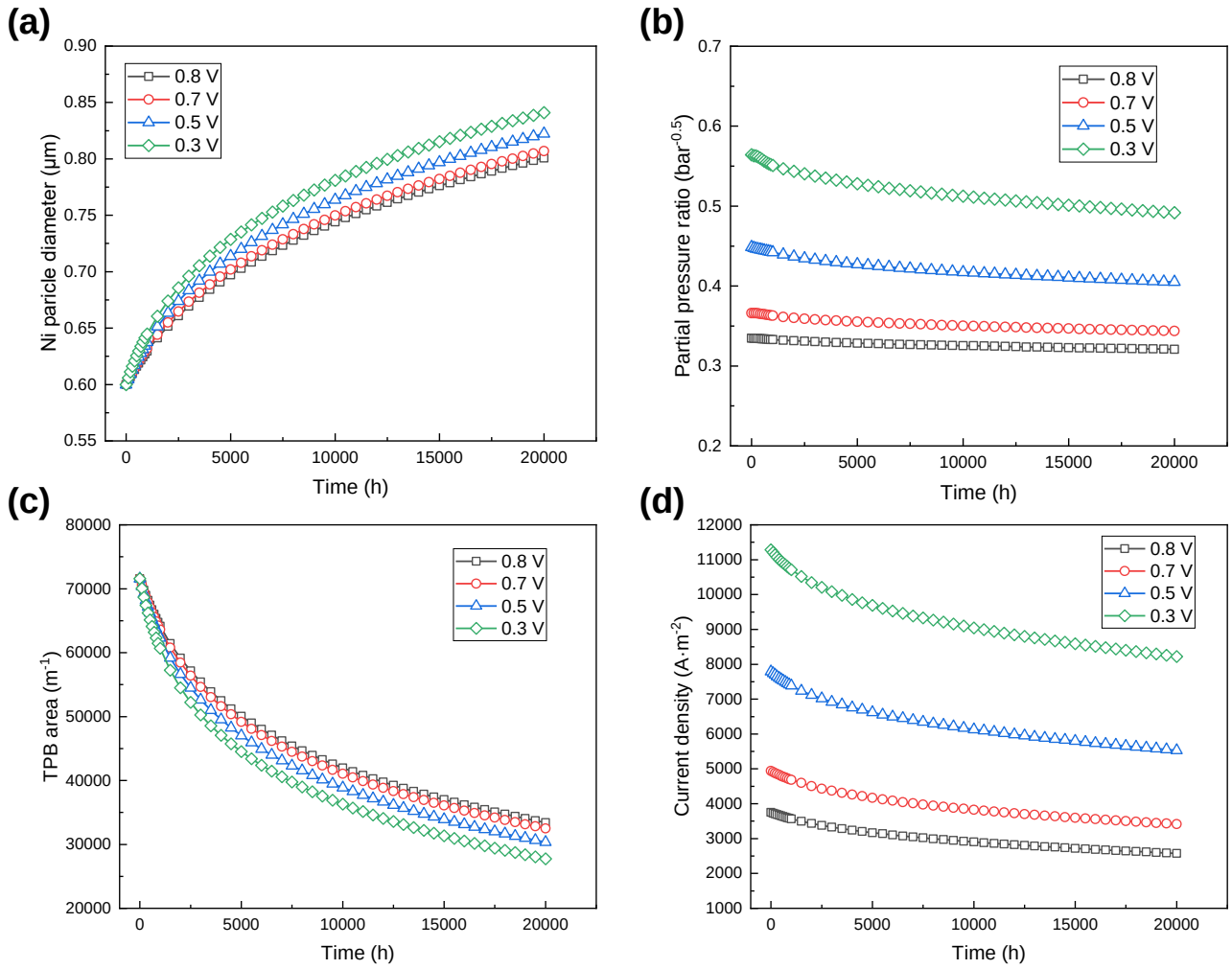


Fig. 8 The effect of operating voltage on (a) Ni particle diameter; (b) partial pressure ratio; (c) effective area of TPB; (d) current density

3.3 The effect of fuel composition

This section discusses the influence of different fuel compositions on SOFC performance attenuation. Herein, a total of five representative cases are discussed, as shown in **Table 3**. These five cases simulate the influence of different S/C ratios on cell performance attenuation by varying the molar fraction of CH_4 and H_2O in syngas atmosphere, respectively. Fig. 9 shows the impact of different fuel compositions on SOFC performance. The different fuel compositions affect the Ni coarsening process mainly by changing the partial pressure ratio. The increase of S/C means that less CH_4 is involved in reforming reaction and less hydrogen is produced, thus increasing the partial pressure ratio, as shown in Fig. 9(b). As a result, the Ni particle coarsening process intensifies and the Ni particle diameter increases, as shown in Fig. 9(a). The three-phase interface area decreases gradually, as shown in Fig. 9(c). With the increase of S/C ratio from 0.5 to 3.0, the Ni particle diameter increases from 0.75

μm to 0.83 μm at t=2 kh. Accordingly, TPB area decreases from 40489 m^{-1} to 29711 m^{-1}. According to the attenuation curve of current density shown in Fig. 9(d), the reduction of S/C ratio helps to decrease the attenuation rate and to increase the average current density. The average current density corresponding to case 1 is 5816 $A \cdot m^{-2}$ and the attenuation rate is 1.1%, while case 5 corresponds to an average current density of 5075 $A \cdot m^{-2}$ with an attenuation rate of 1.6%. In general, reducing the S/C ratio in syngas contributes to suppress Ni particle coarsening, thus improving cell performance.

Table 3 The different fuel compositions

No.	Syngas composition					
	H_2	CO	CO_2	CH_4	H_2O	S/C
Case 1	40%	20%	10%	20%	10%	0.5
Case 2	40%	20%	10%	15%	15%	1.0
Case 3	40%	20%	10%	12%	18%	1.5
Case 4	40%	20%	10%	10%	20%	2.0
Case 5	40%	20%	10%	7.5%	22.5%	3.0

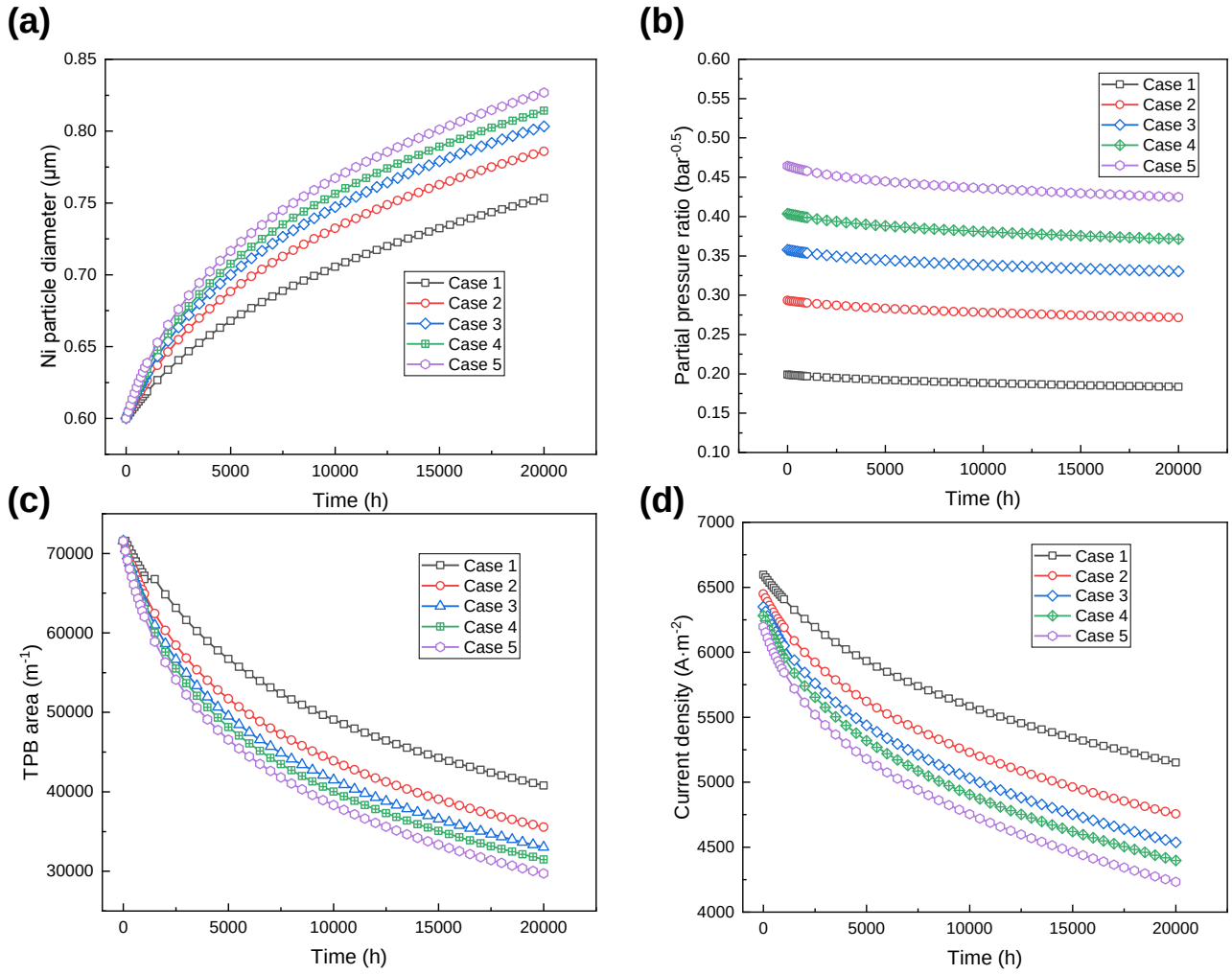


Fig. 9 The effect of fuel composition on (a) Ni particle diameter; (b) partial pressure ratio; (c) effective area of TPB; (d) current density

3.4 The effect of YSZ particle diameter

Fig. 10 shows the influence of different YSZ particle diameters on cell performance attenuation. It can be seen from Fig. 10(a) that decreasing YSZ particle diameter increases the ionic conductive phase surface area, thus hindering the growth of Ni particles. For example, when d_{YSZ}=0.5 μm, A_{io}=4.55 μm, Ni particle diameter is 0.788 μm at t=20 kh; when d_{YSZ}=0.7 μm, A_{io}=3.2 μm, Ni particle diameter is 0.831 μm at t=20 kh. However, the decrease of YSZ particle diameter hinders the connection of electronic conductive phase, which makes the percolation probability decrease rapidly. As shown in Fig. 10(b), when d_{YSZ} exceeds the initial Ni particle diameter d_{Ni0}, P_{el} remains above 0.7; when d_{YSZ} is smaller than the d_{Ni0}, P_{el} decreases rapidly. In particular, when d_{YSZ}=0.5 μm, P_{el} decreases from 0.7 to 0.23 within 2 kh. Fig. 10(c) shows the attenuation curves of TPB area under different YSZ particle diameters. It can be seen that when d_{YSZ}<d_{Ni0}, the TPB area gradually increases with the

increase of d_{YSZ}. When $d_{YSZ}>d_{Ni0}$, TPB area decreases with the improvement of d_{YSZ} in the initial stage but increases in the later stage. This is mainly because in the early stage, percolation probability P_{el} changes relatively little with d_{YSZ}, as depicted in Fig. 10(b), and the decreases of TPB area is mainly controlled by the increase of Ni particle diameter due to the increase of d_{YSZ}. In the later stage, the influence of percolation probability P_{el} on TPB area is gradually remarkable, so TPB area increases with the increase of d_{YSZ}. The complex effect of YSZ particle diameter d_{YSZ} on the TPB area is mainly due to the nonlinear interaction between Ni particles and YSZ particles. In terms of current density, increasing d_{YSZ} will reduce the attenuation rate and increase the average current density. As d_{YSZ} increases from 0.5 μm to 0.7 μm, the attenuation rate decreases from 2.5% to 1.14%, and the average current density increases from 4668 A·m^{-2} to 5238 A·m^{-2}. Therefore, within the currently set range of d_{YSZ}, improving d_{YSZ} is conducive to improving SOFC performance.

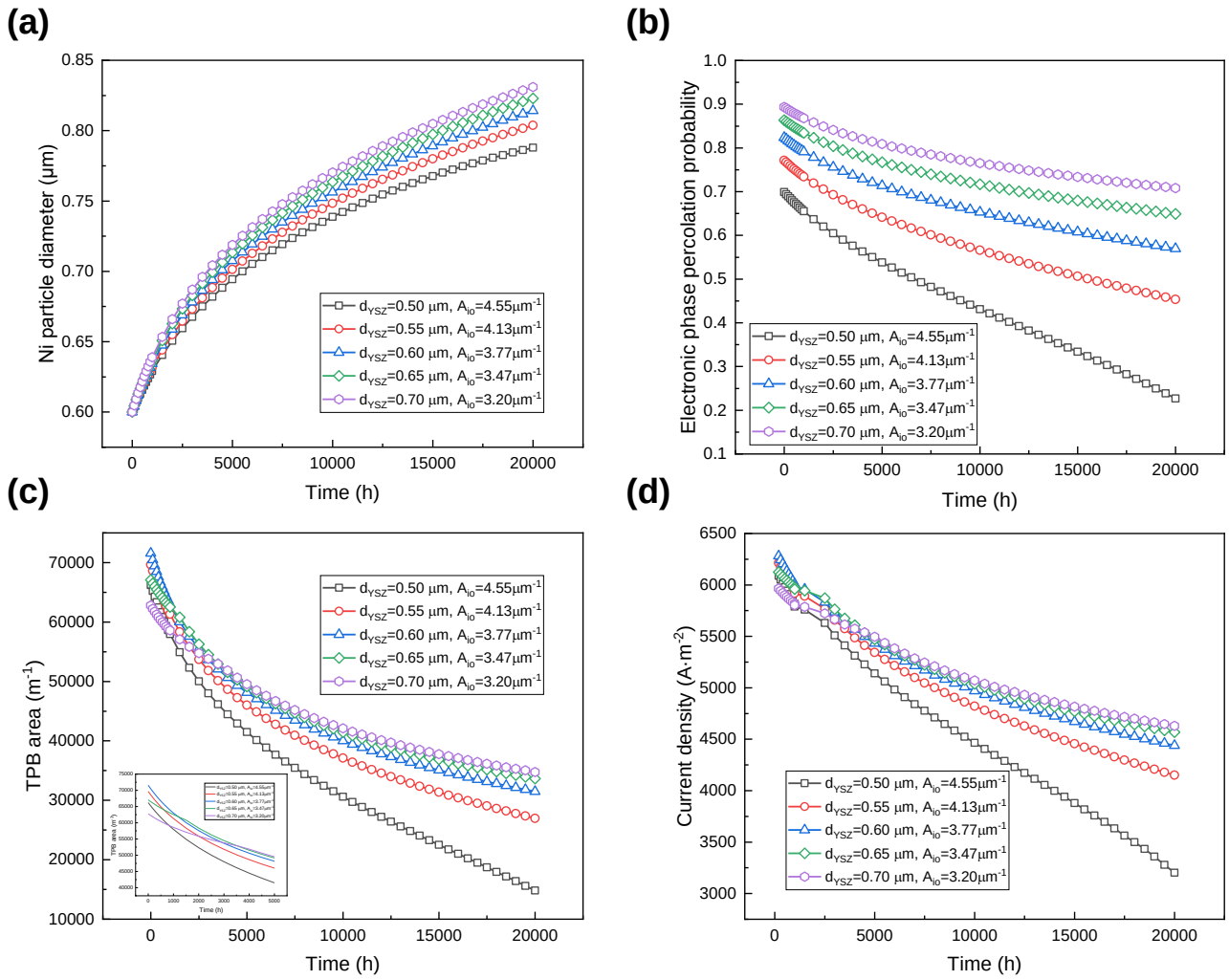


Fig. 10 The effect of YSZ particle diameter on (a) Ni particle diameter; (b) Electronic phase percolation probability; (c) effective area of TPB; (d) current density

3.5 The effect of Ni phase volume fraction

Fig. 11 discusses the impact of different Ni phase fractions ψ_{Ni} on the long-term operating performance of SOFC. It can be seen from Fig. 11(a) that with the increase of ψ_{Ni}, the coarsening rate of Ni particle diameter is significantly accelerated. This is consistent with the phenomenon described by the Ni particle growth formula, as shown in Eq. (22). The increase of ψ_{Ni} also increases the connectivity of electron phase, thus increasing P_{el}, as shown in Fig. 11(b). When ψ_{Ni} increased to more than 0.5, P_{el} remains above 0.85. The increase of P_{el} is not obvious with the increase of ψ_{Ni}. The TPB area increases gradually with the increase of ψ_{Ni}, but the increase is also not obvious when $\psi_{Ni}>0.5$, as shown in Fig. 11(c). This is roughly consistent with the characteristics conveyed in Fig. 11(b). In terms of current density, when ψ_{Ni} is less than 0.45, the current density increases with the increase of ψ_{Ni} throughout the calculation time. But when $\psi_{Ni}>0.45$, the change of current density is not obvious with the increase of ψ_{Ni}. As ψ_{Ni} increases from 0.35 to 0.55, the current density attenuation rate decreases from 3.2% to 0.94%. But when $\psi_{Ni}>0.45$, the decrease of attenuation rate is slight. In a word, increasing Ni phase fraction in a certain range contributes to reducing the attenuation rate of current density, which is beneficial for SOFC long-term operation.

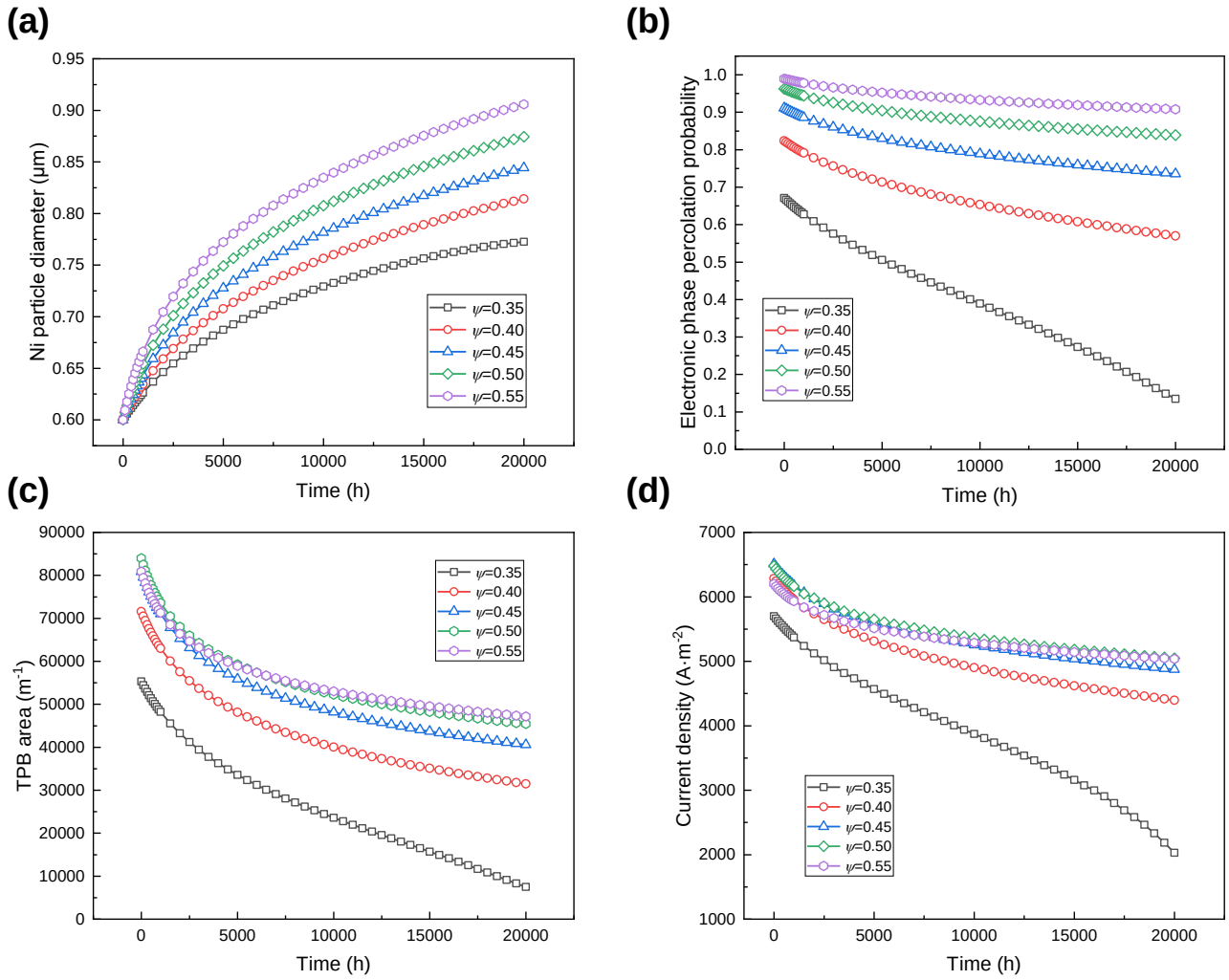


Fig. 11 The effect of Ni phase fraction on (a) Ni particle diameter; (b) electronic phase percolation probability; (c) effective area of TPB; (d) current density.

3.6 ANN prediction

Through the above parametric analyses, it was found that the transient characteristics of SOFC are affected by multiple parameters. Therefore, it is necessary to use ANN to predict the attenuation performance of SOFC. Herein, a total of 6 important parameters including operating temperature, operating voltage, initial Ni particle diameter, YSZ particle diameter, Ni phase fraction, and porosity are selected as input variables of ANN, and two indexes, average current density and attenuation rate, are adopted as output variables of ANN. The value ranges of the input variables are shown in **Table 2**. The training results of ANN are shown in Fig. (12). It can be seen that the value of the output variables is highly linear with the target value. The R index of all samples fitting is 0.999 and the mean square error (MSE) is as low as 4.6E-5. Therefore, it is reliable that the neural network has been trained well and enables to perform the accurate prediction.

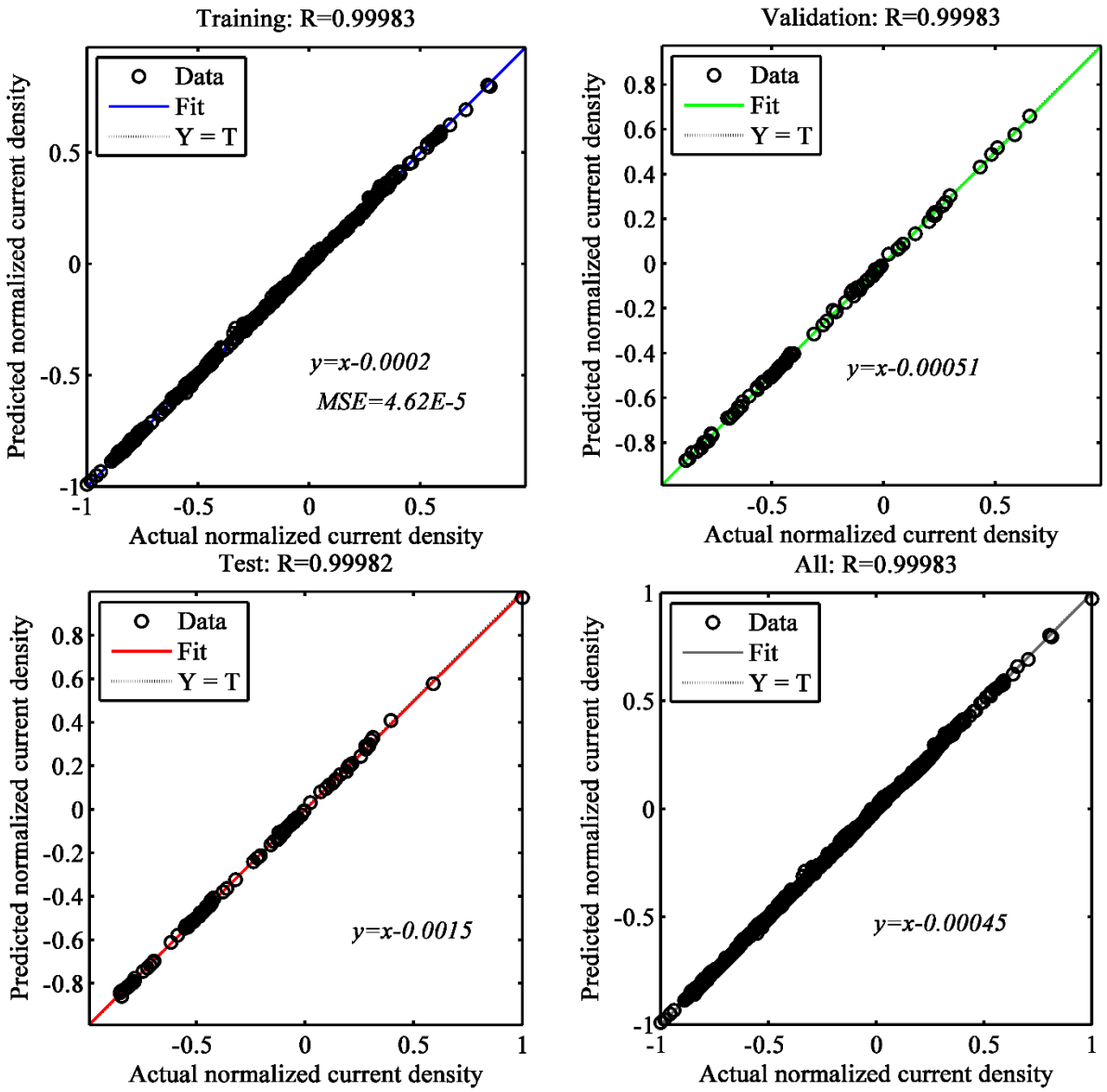


Fig. 12 The performance of ANN training results

First, the attenuation rate of the cell current density is predicted. The relative error between the predicted and the actual values is calculated. The relative error is defined as Eq. (40). Fig. 13 shows the specific prediction results. It can be seen that the relative errors are within the ranges of -3.5%~0.1%, -0.22%~1.2%, -1.1%~1.7%, -1.6%~2.3%, -1.7%~4.4%, -1.6%~0.26% under different temperatures, voltages, initial Ni particle diameters, YSZ particle diameters, Ni phase fractions, porosities, respectively. The average value of absolute relative errors is 0.898%, 0.373%, 1.05%, 0.879%, 0.975%, 0.436%, respectively. The average relative error for all parameters is 0.767%, which is low. The low error also confirms the accuracy and validity of the trained ANN model. Fig. 13 also shows the variation trends of attenuation rate of current density under different parameters. For

example, as the operating temperature increases from 650 to 810 ºC, the attenuation rate increases from 0.22% to 3.7%; as the YSZ particle diameter increases from 0.5 μm to 0.7 μm, the attenuation rate decreases from 2.5% to 1.14%. This trends help us to select parameters more intuitively to meet the requirements of attenuation rate.

$$\mathrm{Re} = \frac{\text{ANN-MPS}}{\text{MPS}} \times 100\% \tag{40}$$

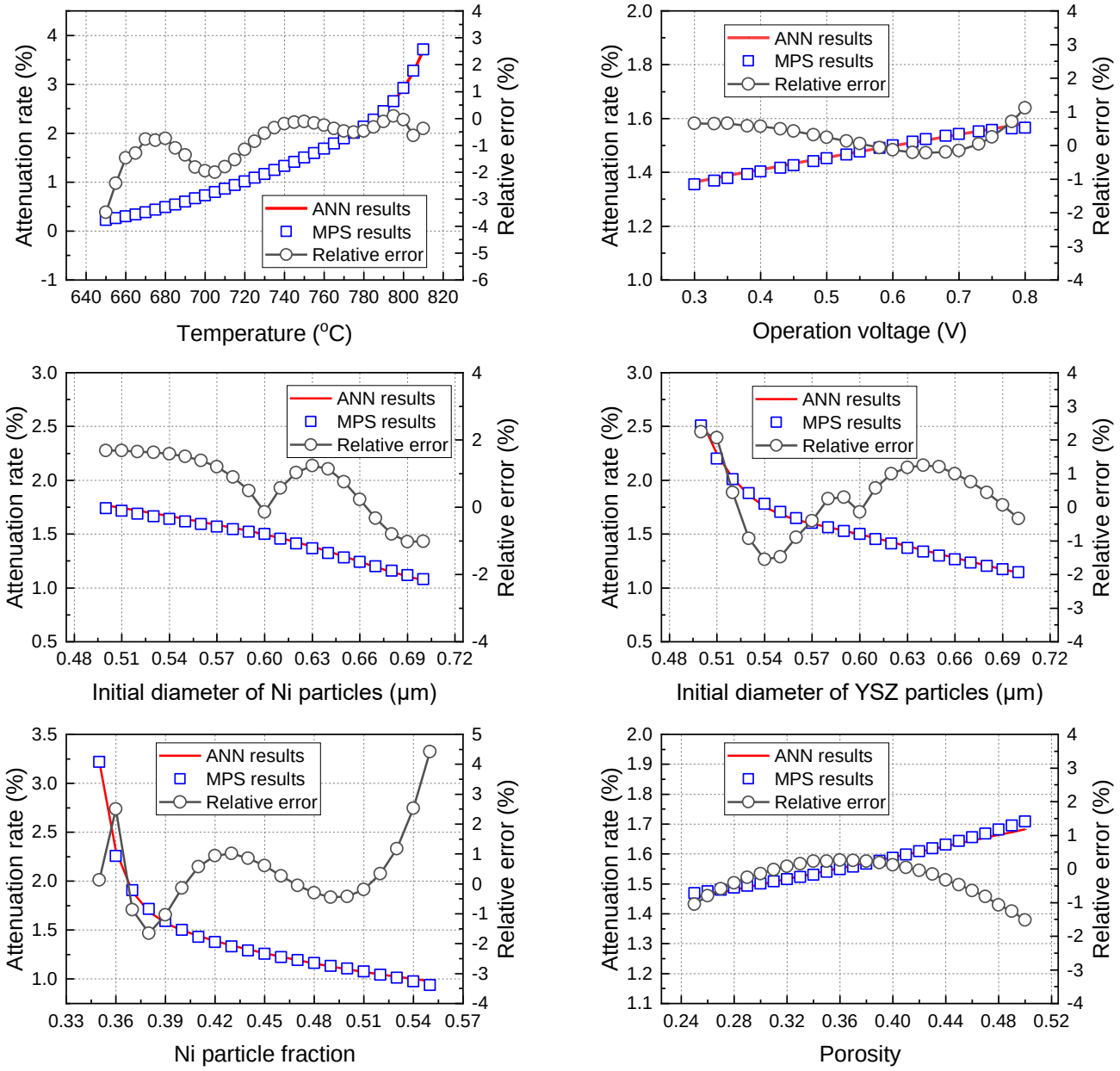


Fig. 13 Comparison of the MPF and ANN models in the prediction of the attenuation rate in SOFCs at different parameters.

The prediction results of average current density are also given by Fig. 14. As can be seen that the relative errors are within the ranges of -0.4%~1.5%, 0~1%, 0.1%~0.6%, -1.0%~0.3%, -0.8%~0.8%,

-0.1%~0.8% under different temperatures, voltages, initial Ni particle diameters, YSZ particle diameters, Ni phase fractions, and porosities, respectively. The average value of absolute relative errors is 0.165%, 0.322%, 0.274%, 0.316%, 0.311%, 0.166%, respectively. Compared with the prediction results of attenuation rate, the error of average current density is lower, which is -1.0%~1.5%. The average relative error of all parameters is 0.248%. This further verifies the accuracy of the ANN predicting the average current density. In addition, the variation trend of average current density under different operating conditions can also be obtained in Fig. 14. It was found that the lowest attenuation rate is often different from the parameters corresponding to the high current density. For example, the temperature of 650 ^{o}C corresponds to the smallest attenuation rate and average current density. By contrast, the attenuation rate and average current density are the highest at 800 ^{o}C. Therefore, it is necessary to conduct optimization for the operating conditions and structural parameters of SOFC to find the optimal operating point that meets the requirements of both low attenuation rate and large current density.

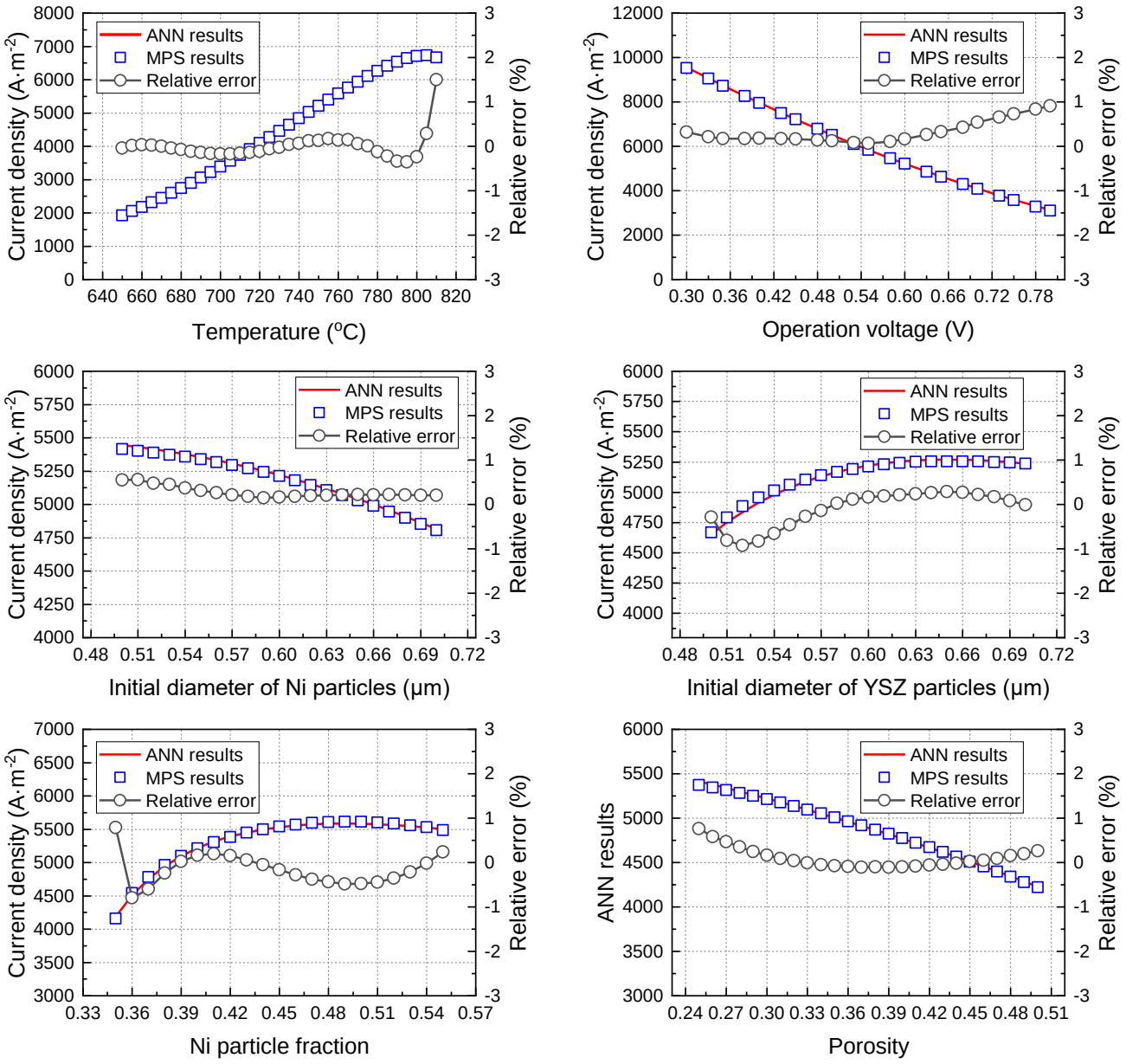


Fig. 14 Comparison of the MPF and ANN models in the prediction of the average density in SOFC at different parameters.

3.7 Optimization SOFC performance with GA

As a source heuristic optimization algorithm, GA is suitable for the optimization problem of without definite function expression. Actually, the GA has been widely used in engineering optimization problem [33,47]. In this optimization problem, ANN mapping is used as fitness function of GA. After the above discussion, it can be found that the parameters corresponding to the minimum attenuation rate and maximum average current density are generally different. The objective of optimization is to seek the maximum average current density but with the attenuation rate of less than

1%. Because the most obvious characterization of SOFC is power density, which is the result of multiplying voltage and current density. So here, the operating voltage is fixed as constant to optimize the current density. When the current density reaches its maximum, the power density also reaches its maximum. The whole optimization problem is summarized as follows.

$$\text{objective function: } \max\left(\bar{I}\right) \tag{41}$$

$$\text{constraint function: } 0<r<1 \tag{42}$$

$$\text{optimization variables} \begin{cases} 650\ ^{o}\text{C}<T<800\ ^{o}\text{C} \\ V \in [0.3\text{V}\ \ 0.8\text{V}] \\ 0.5\ \mu\text{m} \le d_{\text{Ni0}} \le 0.7\ \mu\text{m} \\ 0.5\ \mu\text{m} \le d_{\text{YSZ}} \le 0.7\ \mu\text{m} \\ 0.35 \le \psi_{\text{Ni}} \le 0.55 \\ 0.25 \le \varepsilon_{a} \le 0.5 \end{cases} \tag{43}$$

The optimization results are shown in Fig. 15. Take the optimization result when the operating voltage is 0.6 V as an example to analyze. It can be seen that the GA basically converges at generation about 55. After optimization, the maximum current density is 5848 $\text{A}\cdot\text{m}^{-2}$ under the required attenuation rate. At this time, the corresponding attenuation rate is 0.962% and the optimization variable value vector is (T=759.9, V=0.6, d_{Ni0}=0.693, d_{YSZ}=0.602, ψ_{Ni}=0.50, ε_{a}=0.336). The average current density and attenuation rate calculated by MPF simulation are 5641 $\text{A}\cdot\text{m}^{-2}$ and 0.945%, respectively in the case of current optimized variable. The relative error between MPF simulation results and ANN optimization results is 3.67%. This reflects the reasonableness and reliability of adopting a data-driven approach to optimize SOFC. It is important to note that it may not be necessary to optimize all the parameters listed in Eq. (43) during SOFC practical work or production. In this case, some parameters just need to fix a constant value. In other cases, the parameters that do not appear in Eq. (41) may need to be optimized. In such case, the ANN database needs to be expanded to consider the influence of specific parameters on the value of the objective function, and then the parameters could be optimized by the developed data-driven GA. Fig. (16) shows the evolution of optimization variables during the optimization process. It can be seen that in the process of optimizing the objective function step by step, the optimization variables are constantly evolving. When the objective function gradually stabilizes and approaches the optimal result, the optimization variable is basically stable.

The optimal variables are stable when the generation achieves 40, and the stable optimization variable vector is (T=759.9, V=0.6, d_{Ni0}=0.693, d_{YSZ}=0.602, ψ_{Ni}=0.50, ε_a=0.336).

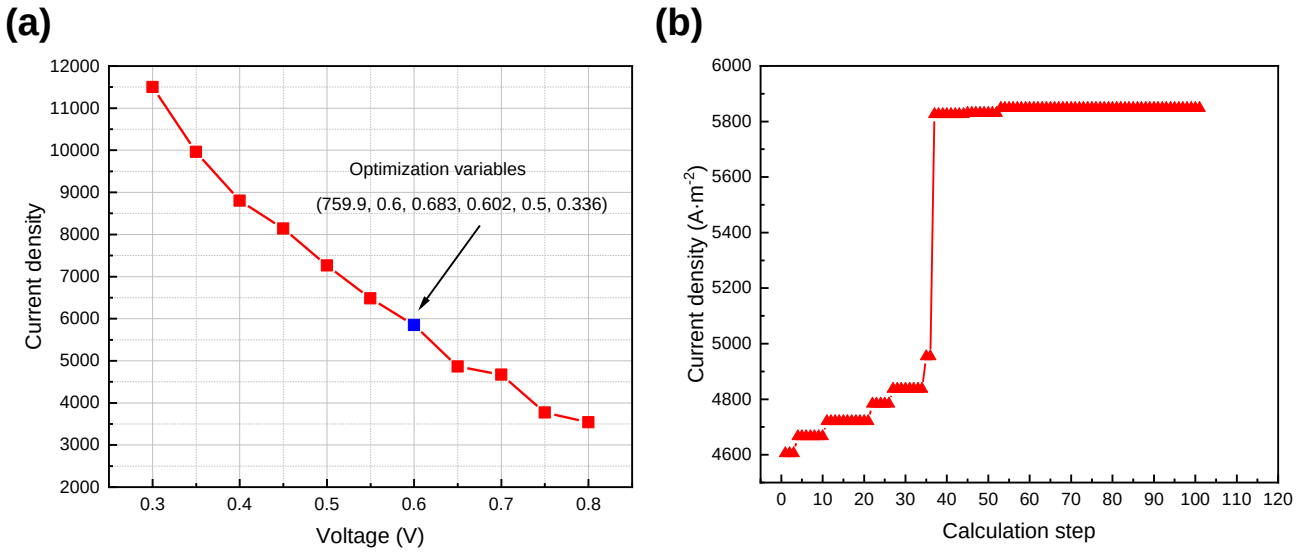


Fig. 15 (a) The optimization results under different operation voltages with the attenuation rate constraint; (b) the GA optimization calculation process diagram under operation voltage at 0.6 V.

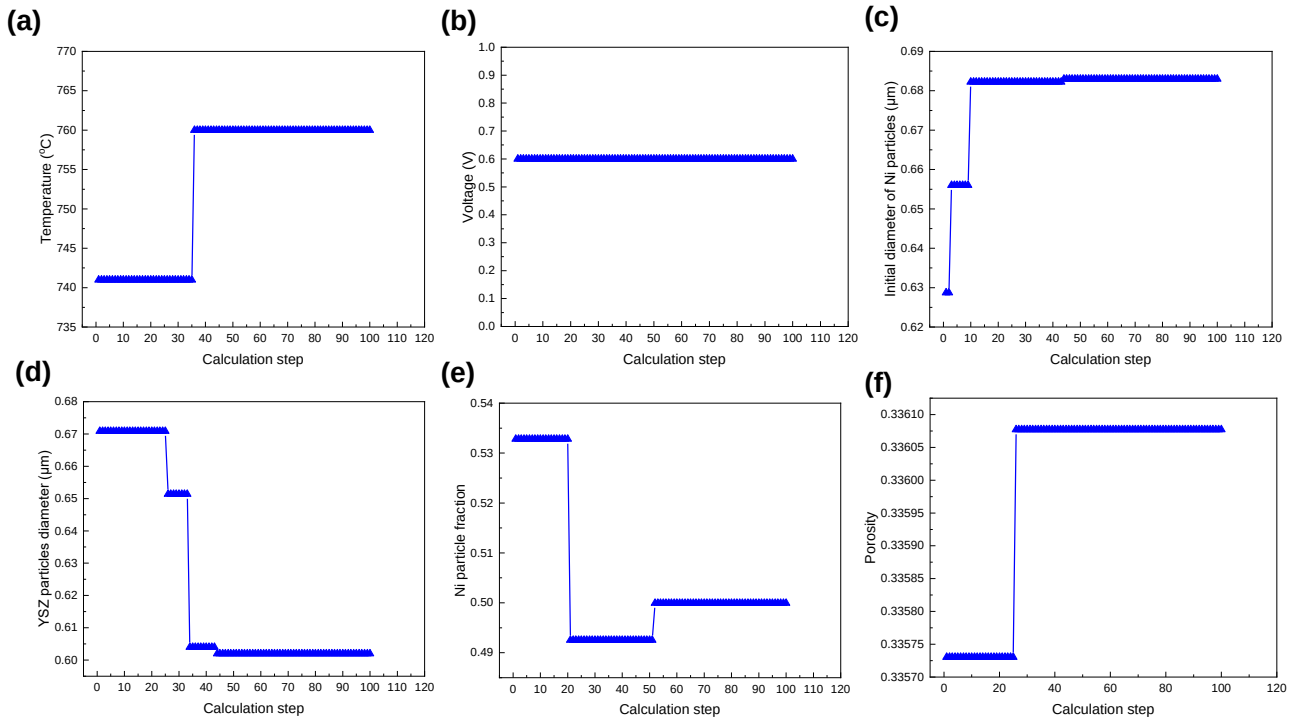


Fig. 16 The evolution of optimization variables in optimization process (a) operation temperature; (b) operation voltage; (c) initial diameter of Ni particles; (d) diameter of YSZ particle; (e) Ni particle fraction; (f) porosity

4. Conclusions

To investigate the influence of Ni particle coarsening on SOFC performance, the SOFC transient multi-physical field model is developed. Additionally, since the calculation time of MPF simulation is too long to achieve fast prediction, ANN is trained by the database generated by MPF simulation. The mapping relationship between parameters (the operating and structural parameters) and attenuation index is obtained. Finally, the attenuation performance of SOFC is optimized by GA. The specific conclusions can be summarized as follows.

- Increasing the operating temperature could improve the current density as a whole. However, the high operating temperature accelerates Ni particle growth and increases attenuation rate of SOFC current density. The attenuation rate is 2.6%/kh at 800 ºC, and 0.23%/kh at 650 ºC. The increase of S/C also intensifies the Ni particle coarsening process and deteriorates the transient performance of SOFC.
- Increasing YSZ particle diameter prevents the growth of Ni particles, which slows down the increase rate of Ni particle diameter. The complex effect of YSZ particle diameter on the TPB area and current density is mainly due to the nonlinear interaction between Ni particles and YSZ particles. In the range of preset YSZ diameter, increasing d_{YSZ} helps to reduce the attenuation rate and to increase the average current density. As the d_{YSZ} increases from 0.5 μm to 0.7 μm, the attenuation rate decreases from 2.5% to 1.14%, and the average current density increases from 4668 $A \cdot m^{-2}$ to 5238 $A \cdot m^{-2}$. When ψ_{Ni} is less than 0.45, the current density increases with the improvement of ψ_{Ni}. But when $\psi_{Ni}>0.45$, the change of current density is slight with the increase of ψ_{Ni}. Increasing Ni phase fraction in a certain range could also reduce the current density attenuation rate.
- The trained ANN is used to predict the average current density and attenuation rate under different operating conditions and structural parameters. The average value of absolute relative errors of all parameters in predicting attenuation rate and average current density is 0.767%% and 0.248%, which indicates the reliability of the ANN prediction.
- The average current density of SOFC is optimized by GA through data-driven method under the condition of limited attenuation rate. The maximum current density is 5701 $A \cdot m^{-2}$ at the fixed attenuation rate. The relative error between MPF simulation results and ANN optimization results

is 1.02% only. The combination of MPF simulation, ANN and GA could provide a framework for fast prediction and optimization of strong nonlinear problems such as complex SOFC multi-physical field.

5. Data and code availability

To ensure the rigor and repeatability of the study, the authors can provide source data and model procedures related to this study upon reasonable request.

Acknowledgement

This work was financially supported by the National Natural Science Foundation of China (No. 52176203 and No. 52050027), the Natural Science Foundation Project of Shaanxi Province, China (No. 2021JQ-890), the Young Talent Fund for Science and Technology in Xi'an City, China (No. 095920211329) and the Guangdong Provincial Key Laboratory of Distributed Energy Systems (No. 2020B1212060075).

Reference

[1] Hepburn C, Qi Y, Stern N, Ward B, Xie C, Zenghelis D. Towards carbon neutrality and China's 14th Five-Year Plan: Clean energy transition, sustainable urban development, and investment priorities. Environ Sci Ecotechnology 2021;8:100130. doi:10.1016/j.ese.2021.100130.

[2] CPC Central Committee and State Council. Opinions on fully, accurately and comprehensively implementing the new development concept to achieve carbon peak and carbon neutral work [In Chinese] 2021. http://www.gov.cn/zhengce/2021-10/24/content_5644613.htm.

[3] International Energy Agency. International Energy Outlook 2021 2021.

[4] He J, Li Z, Zhang X, Wang H, Dong W, Du E, et al. Towards carbon neutrality: A study on China's long-term low-carbon transition pathways and strategies. Environ Sci Ecotechnology 2022;9:100134. doi:10.1016/j.ese.2021.100134.

[5] Choudhury A, Chandra H, Arora A. Application of solid oxide fuel cell technology for power generation—A review. Renew Sustain Energy Rev 2013;20:430–42. doi:10.1016/j.rser.2012.11.031.

[6] Sazali N, Wan Salleh WN, Jamaludin AS, Mhd Razali MN. New Perspectives on Fuel Cell Technology: A Brief Review. Membranes (Basel) 2020;10:99. doi:10.3390/membranes10050099.

[7] Fu Q, Li Z, Wei W, Liu F, Xu X, Liu Z. Performance enhancement of a beam and slot interconnector for anode-supported SOFC stack. Energy Convers Manag 2021;241:114277. doi:10.1016/j.enconman.2021.114277.

[8] Li Q, Chai D, Wang L, Zhang X, Li G. Fine three-dimensional simulation of the heterogeneous anode of a solid oxide fuel cell with direct internal reforming. Chem Eng Sci 2021;242:116747. doi:10.1016/j.ces.2021.116747.

[9] Zhu P, Wu Z, Yao J, Guo L, Yan H, Nyamsi SN, et al. Multi-physics field modeling of biomass gasification syngas fueled solid oxide fuel cell. J Power Sources 2021;512:230470. doi:10.1016/j.jpowsour.2021.230470.

[10] Xu Q, Xia L, He Q, Guo Z, Ni M. Thermo-electrochemical modelling of high temperature methanol-fuelled solid oxide fuel cells. Appl Energy 2021;291:116832. doi:10.1016/j.apenergy.2021.116832.

[11] Elleuch A, Halouani K, Li Y. Bio-methanol fueled intermediate temperature solid oxide fuel cell: A future solution as component in auxiliary power unit for eco-transportation. Mater Des 2016;97:331–40. doi:10.1016/j.matdes.2016.02.060.

[12] Afif A, Radenahmad N, Cheok Q, Shams S, Kim JH, Azad AK. Ammonia-fed fuel cells: a comprehensive review. Renew Sustain Energy Rev 2016;60:822–35. doi:10.1016/j.rser.2016.01.120.

[13] Cinti G, Discepoli G, Sisani E, Desideri U. SOFC operating with ammonia: Stack test and system analysis. Int J Hydrogen Energy 2016;41:13583–90. doi:10.1016/j.ijhydene.2016.06.070.

[14] Zhu P, Wu Z, Guo L, Yao J, Dai M, Ren J, et al. Achieving high-efficiency conversion and poly-generation of cooling, heating, and power based on biomass-fueled SOFC hybrid system: Performance assessment and multi-objective optimization. Energy Convers Manag 2021;240:114245. doi:10.1016/j.enconman.2021.114245.

[15] Somano V, Ferrero D, Santarelli M, Papurello D. CFD model for tubular SOFC directly fed by biomass. Int J Hydrogen Energy 2021;46:17421–34. doi:10.1016/j.ijhydene.2021.02.147.

[16] Kong W, Han Z, Lu S, Gao X, Wang X. A novel interconnector design of SOFC. Int J Hydrogen Energy 2020;45:20329–38. doi:10.1016/j.ijhydene.2019.10.252.

[17] Hubert M, Laurencin J, Cloetens P, Morel B, Montinaro D, Lefebvre-Joud F. Impact of Nickel agglomeration on solid oxide cell operated in fuel cell and electrolysis modes. J Power Sources 2018;397:240–51. doi:10.1016/j.jpowsour.2018.06.097.

[18] Mason J, Celik I, Lee S, Abernathy H, Hackett G. Performance Degradation Predictions Based on Microstructural Evolution Due to Grain Coarsening Effects in Solid Oxide Fuel Cell Electrodes. J Electrochem Soc 2018;165:F64–74. doi:10.1149/2.0721802jes.

[19] Peng J, Huang J, Wu X, Xu Y, Chen H, Li X. Solid oxide fuel cell (SOFC) performance evaluation, fault diagnosis and health control: A review. J Power Sources 2021;505:230058. doi:10.1016/j.jpowsour.2021.230058.

[20] Miyoshi K, Iwai H, Kishimoto M, Saito M, Yoshida H. Chromium poisoning in (La,Sr)MnO3 cathode: Three-dimensional simulation of a solid oxide fuel cell. J Power Sources 2016;326:331–40. doi:10.1016/j.jpowsour.2016.06.110.

[21] Liu YL, Hagen A, Barfod R, Chen M, Wang HJ, Poulsen FW, et al. Microstructural studies on degradation of interface between LSM–YSZ cathode and YSZ electrolyte in SOFCs. Solid State Ionics 2009;180:1298–304. doi:10.1016/j.ssi.2009.07.011.

[22] Coors WG, O'Brien JR, White JT. Conductivity degradation of NiO-containing 8YSZ and 10YSZ electrolyte during reduction. Solid State Ionics 2009;180:246–51. doi:10.1016/j.ssi.2008.12.004.

[23] Larrain D, Van herle J, Favrat D. Simulation of SOFC stack and repeat elements including interconnect degradation and anode reoxidation risk. J Power Sources 2006;161:392–403. doi:10.1016/j.jpowsour.2006.04.151.

[24] Han M, Li Z, Du X, Chen X. Development of coating materials on alloy interconnect in solid oxide fuel cell [In Chinese]. Rare Met Mater Eng 2009;38:708–11. doi:10.3321/j.issn:1002-185X.2009.z2.189.

[25] Ma T, Yan M, Zeng M, Yuan J, Chen Q, Sundén B, et al. Parameter study of transient carbon deposition effect on the performance of a planar solid oxide fuel cell. Appl Energy 2015;152:217–28. doi:10.1016/j.apenergy.2014.11.061.

[26] Liu M, Millan MG, Aravind P V., Brandon N. Influence of Operating Conditions on Carbon Deposition in SOFCs Fuelled by Tar-Containing Biosyngas. J Electrochem Soc 2011;158:B1310. doi:10.1149/2.027111jes.

[27] Zhang R, Wang Y, Shi Y, Wang Y, Cao H. Elementary Reaction Kinetic Model of an Anode-Supported Syngas Fueled Solid Oxide Fuel Cell Considering the Carbon Deposition Effect. ECS Trans 2021;103:949–57. doi:10.1149/10301.0949ecst.

[28] Schluckner C, Subotić V, Lawlor V, Hochenauer C. Carbon Deposition Simulation in Porous SOFC Anodes: A Detailed Numerical Analysis of Major Carbon Precursors. J Fuel Cell Sci Technol 2015;12. doi:10.1115/1.4031862.

[29] Fu Q, Li Z, Wei W, Liu F, Xu X, Liu Z. Performance degradation prediction of direct internal reforming solid oxide fuel cell due to Ni-particle coarsening in composite anode. Energy Convers Manag 2021;233:113902. doi:10.1016/j.enconman.2021.113902.

[30] Sehested J. Sintering of nickel steam-reforming catalysts: effects of temperature and steam and hydrogen pressures. J Catal 2004;223:432–43. doi:10.1016/j.jcat.2004.01.026.

[31] Zhu J, Lin Z. Degradations of the electrochemical performance of solid oxide fuel cell induced by material microstructure evolutions. Appl Energy 2018;231:22–8. doi:10.1016/j.apenergy.2018.09.127.

[32] Babaie Rizvandi O, Miao X-Y, Frandsen HL. Multiscale modeling of degradation of full solid oxide fuel cell stacks. Int J Hydrogen Energy 2021;46:27709–30. doi:10.1016/j.ijhydene.2021.05.204.

[33] Xu H, Ma J, Tan P, Chen B, Wu Z, Zhang Y, et al. Towards online optimisation of solid oxide fuel cell performance: Combining deep learning with multi-physics simulation. Energy AI 2020;1:100003. doi:10.1016/j.egyai.2020.100003.

[34] Fu Q, Li Z, Wei W, Liu F, Xu X, Liu Z. Performance enhancement of planar solid oxide fuel cell using a novel interconnector design. Int J Hydrogen Energy 2021;46:21634–56. doi:10.1016/j.ijhydene.2021.04.001.

[35] Sohn S, Baek SM, Nam JH, Kim C-J. Two-dimensional micro/macroscale model for intermediate-temperature solid oxide fuel cells considering the direct internal reforming of methane. Int J Hydrogen Energy 2016;41:5582–97. doi:10.1016/j.ijhydene.2016.01.161.

[36] Zhu P, Yao J, Wu Z, Huang S-M, Radzi Abu Mansor M, Yang F, et al. Construction of a transient multi-physics model of solid oxide fuel cell fed by biomass syngas considering the carbon deposition and temperature effect. Chem Eng J 2022;442:136159. doi:10.1016/j.cej.2022.136159.

[37] Jing X, Mingyi X, Shuai B, Hui S, Hongjun Z. Simulation analysis of multi-physics coupling SOFC fueled nature gas in the way of internal reforming and external reforming. CIESC J 2019;70:214–26.

[38] Xu Q, Ni M. Modelling of high temperature direct methanol solid oxide fuel cells. Int J Energy Res 2021;45:3097–112. doi:10.1002/er.6003.

[39] Li Z, Yang G, Li S, Shen Q, Yang F, Wang H, et al. Modeling and analysis of microchannel autothermal methane steam reformer focusing on thermal characteristic and thermo-mechanically induced stress behavior. Int J Hydrogen Energy 2021;46:19822–34. doi:10.1016/j.ijhydene.2021.03.118.

[40] Pantoleontos G, Kikkinides ES, Georgiadis MC. A heterogeneous dynamic model for the

simulation and optimisation of the steam methane reforming reactor. Int J Hydrogen Energy 2012;37:16346–58. doi:10.1016/j.ijhydene.2012.02.125.

[41] Yahya A, Ferrero D, Dhahri H, Leone P, Slimi K, Santarelli M. Electrochemical performance of solid oxide fuel cell: Experimental study and calibrated model. Energy 2018;142:932–43. doi:10.1016/j.energy.2017.10.088.

[42] Zhu J. Performance degradation modeling and non-coking anode design of solid oxide fuel cell[In Chinese]. University of Science and Technology of China, 2018.

[43] Chen D, Lin Z, Zhu H, Kee RJ. Percolation theory to predict effective properties of solid oxide fuel-cell composite electrodes. J Power Sources 2009;191:240–52. doi:10.1016/j.jpowsour.2009.02.051.

[44] Grew KN, Joshi AS, Peracchio AA, Chiu WKS. Pore-scale investigation of mass transport and electrochemistry in a solid oxide fuel cell anode. J Power Sources 2010;195:2331–45. doi:10.1016/j.jpowsour.2009.10.067.

[45] Völker B, McMeeking RM. Impact of particle size ratio and volume fraction on effective material parameters and performance in solid oxide fuel cell electrodes. J Power Sources 2012;215:199–215. doi:10.1016/j.jpowsour.2012.05.014.

[46] Sun Y, Lu J, Liu Q, Shuai W, Sun A, Zheng N, et al. Multi-objective optimizations of solid oxide co-electrolysis with intermittent renewable power supply via multi-physics simulation and deep learning strategy. Energy Convers Manag 2022;258:115560. doi:10.1016/j.enconman.2022.115560.

[47] Xu H, Ma J, Tan P, Wu Z, Zhang Y, Ni M, et al. Enabling thermal-neutral electrolysis for CO2-to-fuel conversions with a hybrid deep learning strategy. Energy Convers Manag 2021;230:113827. doi:10.1016/j.enconman.2021.113827.